


Image Cover Sheet

CLASSIFICATION UNCLASSIFIED	SYSTEM NUMBER 61396 
---	---

TITLE
CRUSTAL MAGNETIZATION AND GRADIENT TENSOR COMPONENT MAPS OF THE
NORTHERN JUAN DE FUCA RIDGE

System Number:

Patron Number:

Requester:

Notes:

DSIS Use only: Deliver to: JR
--



Defence Research
Establishment Pacific

Centre de recherches
pour la defense pacifique

DEFENCE RESEARCH ESTABLISHMENT P. 100

CFB Esquimalt, FMO Victoria, B.C. VOS 1B0

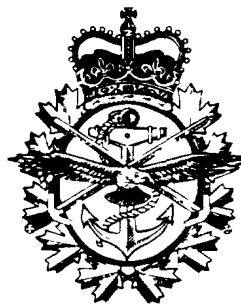
Technical Memorandum 88-21

CRUSTAL MAGNETIZATION AND GRADIENT TENSOR COMPONENT

OF THE NORTHERN JUAN DE FUCA RIDGE

J. Bradley Nelson

November 1988



Approved

J. G.

Research and Development Branch
Department of National Defence

Canada

ABSTRACT

Computer simulations of airborne magnetic detection systems require accurate models for various background noise sources, including aircraft interference, geomagnetic micropulsation and geological sources. Previous measurements of geological background signals have been restricted to a few flights through the region of interest. Because of the inherent one dimensional nature of the data, the resulting models do not accurately reflect the spatial coherence of the geological noise during aircraft manoeuvres. To improve the models, surveys must consist of many closely spaced flight lines.

Geological noise models can be developed either from measurements of the quantities of interest over a specific area, or as estimates of the magnetization and geometry of the underlying source from which the quantities can be calculated directly. For simulations of SQUID sensors, the quantities of interest are the magnetic gradient tensor components $g_{\alpha\beta} = \partial B_{\alpha} / \partial x_{\beta}$ (the spatial derivative of magnetic field vector component α in the direction β). A method for calculating these tensor components from measurements of the total-field (or its vertical or horizontal derivatives) throughout a plane is presented.

//An aeromagnetic survey over the northern Juan de Fuca Ridge has been completed for DREP by the National Aeronautical Establishment. Measurements of the total-field and its derivatives in both the vertical and horizontal directions were taken at an altitude of 300 m above sea-level, with a nominal line spacing of 1.8 km. Contour maps of the five independent components of the gradient tensor generated from the horizontal derivative data, and a model of the geological magnetization based on the total-field measurements and existing bathymetry maps are presented. //

TABLE OF CONTENTS

ABSTRACT.....	iii
LIST OF FIGURES.....	vi
1. INTRODUCTION.....	1
2. ANALYSIS METHODS.....	3
3. DATA.....	6
4. CONCLUSIONS.....	34
5. REFERENCES.....	36
6. APPENDICES.....	38
A: INTEGRAL RELATIONS BETWEEN TENSOR GRADIENT COMPONENTS..	A1
B: RELATIONS BETWEEN THE TOTAL-FIELD, THE TOTAL-FIELD DERIVATIVES, AND THE GRADIENT TENSOR: FREQUENCY DOMAIN.....	B1
C: CALCULATION OF THE MAGNETIZATION.....	C1

LIST OF FIGURES

Figure 1. Total-field over entire area, showing aircraft lines. (Altitude is 300 m, units are nT).....	7
Figure 2. Along-track, across-track and vertical derivative measurements along a single profile.....	8
Figure 3(a). Contour plot of g_{nn} over region A (300 m, units are nT/m).....	9
Figure 3(b). Contour plot of g_{nn} over region B (300 m, units are nT/m).....	10
Figure 4(a). Contour plot of g_{ne} over region A (300 m, units are nT/m).....	11
Figure 4(b). Contour plot of g_{ne} over region B (300 m, units are nT/m).....	12
Figure 5(a). Contour plot of g_{nv} over region A (300 m, units are nT/m).....	13
Figure 5(b). Contour plot of g_{nv} over region B (300 m, units are nT/m).....	14
Figure 6(a). Contour plot of g_{ev} over region A (300 m, units are nT/m).....	15
Figure 6(b). Contour plot of g_{ev} over region B (300 m, units are nT/m).....	16

Figure 7(a). Contour plot of g_{VV} over region A (300 m, units are nT/m).....	17
Figure 7(b). Contour plot of g_{VV} over region B (300 m, units are nT/m).....	18
Figure 8(a). Surface grid plot of g_{NN} over region A (300 m).....	20
Figure 8(b). Surface grid plot of g_{NN} over region B (300 m).....	21
Figure 9(a). Surface grid plot of g_{Ne} over region A (300 m).....	22
Figure 9(b). Surface grid plot of g_{Ne} over region B (300 m).....	23
Figure 10(a). Surface grid plot of g_{NV} over region A (300 m).....	24
Figure 10(b). Surface grid plot of g_{NV} over region B (300 m).....	25
Figure 11(a). Surface grid plot of g_{eV} over region A (300 m).....	26
Figure 11(b). Surface grid plot of g_{eV} over region B (300 m).....	27
Figure 12(a). Surface grid plot of g_{VV} over region A (300 m).....	28
Figure 12(b). Surface grid plot of g_{VV} over region B (300 m).....	29
Figure 13. Bathymetric contour plot of entire area (units are m)....	30
Figure 14. Magnetization estimate for entire area (units are nT)....	31
Figure 15. Contour plot of the power spectrum of total-field measurements over region A (units are dB relative to arbitrary units).....	34

1. INTRODUCTION

Magnetic anomaly detection uses airborne magnetometers to sense the perturbation in the Earth's magnetic field caused by a submarine. This perturbation moves slowly through space along with the submarine, but because the sensor is moving through the perturbation quite rapidly, the signal appears as a transient. The spectral content of this time varying signal is a function of the aircraft speed; for a CP-140 travelling at 100 m/s, almost all of the power lies between 0 and 0.5 Hz. Thus the shortest wavelength of interest ($\lambda=v/f$) is about 200 m.

Computer simulations of inboard-MAD equipped helicopters and towed SQUID gradiometer systems are being developed at DREP. Both must have accurate models for the various background noise sources, including geological noise. The Geological Survey of Canada (GSC) has produced a wide variety of magnetic contour maps of Canada's coastal waters but unfortunately, they are often based on sparsely sampled shipborne data and gridded at intervals of at least 1 km. While these maps are adequate for the study of large scale anomalies in the crustal magnetization, they are not adequate for modelling geological noise sources because they contain very little information with wavelengths shorter than 2 km. Over the past few years, DREP has collected high resolution geological magnetic signals (10-20 m sample spacing) from a variety of magnetic environments including the deep ocean, continental shelves and Arctic channels. The early DREP geological magnetic measurements were collected either by flying individual survey lines across the region of interest, or by flying patterns similar to ASW submarine hunting and tracking manoeuvres (e.g. trapping circles or cloverleaves). Unfortunately, these data do not accurately reflect the two-dimensional spatial coherence of the magnetic signals during these manoeuvres.

To make the geological noise models more accurate, it is necessary to collect magnetic data in two dimensions. Instead of single profiles across the region of interest, a set of closely spaced survey lines which covers the entire area must be flown. Because the along-track sampling interval

can be made much smaller than the spacing between the survey lines, it would be desirable to fly a set of closely spaced lines in each direction. However, the cost of performing two surveys makes this approach impractical for any large region of interest. Instead, DREP has chosen to fly a single set of survey lines, with the minimum line spacing that the accuracy of the navigation systems permit, and a few tie lines perpendicular to the survey lines to verify the across-track integrity of the data.

The first closely spaced magnetic survey undertaken by DREP was over the Juan de Fuca Ridge, from 47°56'-48°40'N and 128°-130°W. This region contains several diverse topographical features including a sea-floor spreading centre, seamount chains and thickly sedimented valleys. The survey was performed with the National Aeronautical Establishment's Convair 580 aircraft, equipped with three cesium vapour magnetometers (one on each wingtip and one on the tail). The difference between the wingtips yielded the lateral derivative; the difference between the tail and average of the wingtips yielded the vertical derivative; the time derivative of the port magnetometer signal divided by the ground speed yielded the along-track derivative. Thus measurements of the total-field, and the north, east and vertical derivatives of the total-field, were obtained.

The survey consisted of 56 individual lines with a total length of approximately 8000 km. The sampling interval along each line was approximately 1 data point every 15 metres. The line spacing was (nominally) 1.8 km and the flight altitude was 300 m. Bathymetry maps indicate that the average water depth is 2.5 km in the survey area, so the average depth-to-source was 2.8 km.

Litton LTN-51 (inertial navigation), Loran-C, and Global Navigation System (GNS) data were combined using a Kalman filter technique to produce the best estimate of the aircraft position.

A ground station was set up at CFAD Rocky Point to monitor the micropulsation level during the survey flights. The micropulsation level was found to be so low that correction of the aeromagnetic data for this noise source was not required.

2. ANALYSIS METHODS

There are two possible methods for developing geological noise models: one based on measurements of the particular magnetic quantity of interest; and one based on determining the geometry and magnetization of the underlying sources. For simulations of inboard-MAD equipped helicopters, the measured quantity is the total magnetic field, while for simulations of SQUID gradiometers, the measured quantity is the gradient tensor $g_{\alpha\beta} = \partial B_{\alpha} / \partial x_{\beta}$ (the spacial gradient of the magnetic field component B_{α} in the direction β). No device, except a SQUID gradiometer, can yield low noise measurements of the gradient tensor directly.

However, it can be shown that if either the total-field, the vertical derivative, or both components of the horizontal derivative are measured on a horizontal surface, then the other quantities can be calculated on that surface as well (Nabighian, 1984; Nelson, 1986). In addition, if the direction of the Earth's magnetic field is known, then the components of the magnetic gradient tensor can be calculated (Nelson, 1987). It is also well known that magnetic measurements on a horizontal plane can be upward or downward-continued to any other parallel plane (Henderson and Zeitz, 1949, Henderson, 1970). i.e. the total-field at one height can be calculated from total-field measurements taken at another height. Thus, in principle, if the total-field is measured on a horizontal surface, all spatial derivatives of the field (or its components if the direction of the Earth's field is known) can be calculated anywhere in space except at the location of the source. In practise, however, there are boundary effects, noise in the measurements, finite sampling intervals and errors in the altitude and position data. These limit the accuracy and resolution of all the calculated quantities. Refer to Appendices A and B for the mathematical framework required to calculate the gradient tensor components from measurements of the total-field or its derivatives.

The other modelling technique assumes a magnetic source layer of constant thickness. The magnetization is assumed to be constant with depth, but is allowed to vary in strength horizontally. If the top of the magnetic layer is at a constant depth, and the direction of magnetization is known,

then deconvolution techniques can be used to estimate the strength of the magnetization from measurements of any one of the magnetic quantities on a horizontal surface above this layer (Schouten and McCamy, 1972). If the magnetic layer has some relief, but the thickness is still constant, then an iterative deconvolution method can be applied (Parker and Huestis, 1974). These deconvolution methods are much faster than matrix inversion methods because they utilize the fast Fourier transform. Refer to Appendix C for a mathematical description of these methods.

Several problems arise when one tries to use the iterative deconvolution method to calculate the crustal magnetization. First, the depth, thickness and topography of the magnetic basement are not well defined. The thickness of the magnetized layer is difficult to determine but other researchers have used 500 metres as a representative value (Atwater and Mudie, 1973; Klitgord et al., 1975). The depth and topography can be approximated by the bathymetry because the sediment cover is quite thin over most of the survey area (McManus et al., 1972). In addition, all magnetic inversion methods suffer from non-uniqueness, that is, there is a whole family of magnetization distributions which produce no measurable signal on the surface where the measurements are taken. Thus the actual magnetization distribution could be the sum of the deconvolution estimate plus any member of this family. Finally, the gridding routine can produce peculiar anomalies in the gridded data. These measurements were gridded using an iterative Laplace polynomial interpolation routine obtained from Dr. Paul Johnson from the University of Washington, School of Oceanography. The grid mesh was 148 m (east) \times 222 m (north) which corresponds to $.002^\circ \times .002^\circ$ in longitude and latitude. This algorithm was used because it was much faster than other, more complex, gridding algorithms; unfortunately it is known to create oscillations in the sparsely sampled direction. Thus, one should not have too much confidence in any north-south oscillations in the gridded data sets.

The two models for geological noise over the Northern Juan de Fuca Ridge can be used as input for computer simulations of MAD or SQUID gradiometer systems. While the maps could be input as five grids of spatial magnetic measurements, it would probably be more efficient to input only the

power and phase spectra of g_{VV} ($= \partial B_{\text{vertical}} / \partial z$) and derive the other components with equations (B13)-(B21). In addition, the power spectra "P" of any gradient component at an altitude "h", other than the altitude "z₀" at which it was measured, is given by (Henderson and Zeitz, 1949)

$$P(k_x, k_y, h) = \exp(-2k(h-z_0))P(k_x, y, z_0) , \quad (1)$$

where k_x and k_y are the wavenumbers in the x and y directions respectively, and $k^2 = (k_x^2 + k_y^2)$. Thus, if the simulation requires a flight altitude other than 300 m above sea-level, the power spectrum of g_{VV} can be calculated at the desired altitude via equation (1). The other tensor components can then be derived from the upward-continued, or downward-continued, g_{VV} . If the spatial sampling rate used in the simulation is different from that in the maps, the power and phase spectra of the map can be "zero-filled" out to the appropriate wavenumbers. When inverse Fourier transformed, this results in an interpolated grid of tensor component measurements.

The magnetization and bathymetry models are best input into simulations in the wavenumber domain also. The Fourier transform of the total-field anomaly "FFT(tf)" due to a layer of magnetized material is given by (Parker, 1972)

$$\text{FFT}(tf) = e^{-kz_0} (\hat{B}_e \cdot \vec{K}) (\hat{M}_0 \cdot \vec{K}) (1 - e^{-kh_0}) \sum_{n=0}^{\infty} \frac{k^{n-2}}{n!} \text{FFT}(M(\vec{r})h^n(\vec{r})) \quad (2)$$

where z_0 is the average depth to the magnetic layer,

\hat{B}_e is a unit vector in the direction of the Earth's field,

$\vec{K} = (ik_x, ik_y, k)$,

\hat{M}_0 is a unit vector in the direction of the magnetization,

h_0 is the thickness of the layer,

$M(\vec{r})$ is the strength of the magnetization at the location \vec{r} , and

$h(\vec{r})$ is the variation in topography at the location \vec{r} .

Equation (2) can be used to calculate the total-field anomaly for any

thickness and depth of magnetic layer, for any magnetic latitude, given the magnetization "M" and topography "h". In addition, the magnetization of the Juan de Fuca Ridge is probably representative of many sea-floor spreading areas. By combining the model for the Juan de Fuca magnetization with bathymetry data from other spreading zones, new geological magnetic models can be developed. Zero-filling of the high-frequency part of the Fourier transform can also be used to generate magnetic data on a finer grid if so required by the simulation.

The Fourier transform of the vertical derivative of the total-field is related to the Fourier transform of the total-field by (Nabighian, 1984)

$$\text{FFT}(G_z) = k \text{FFT}(tf) . \quad (3)$$

Using equations (2), (3), B(11), (B25), and (B13)-(B21), the total-field, the vertical and horizontal derivatives of the total-field, and all tensor gradient components can be calculated from the magnetization and topography.

3. DATA

Figure 1 is a colour-fill contour plot of the total-field, showing the aircraft flight lines used in this survey. The units of magnetic field intensity are nT (1 nT=1 gamma). The upper rectangular area from 48.220° to 48.660°N, and 128° to 130°W, and the lower rectangular area from 47.940° to 48.218°N, from 128.5° to 129.5°W were analysed separately; in subsequent figures "(a)" and "(b)" refer to the upper and lower regions respectively.

Figure 2 is a plot of the along-track, across-track and vertical derivative measurements (in gammas/metre) along a representative profile. The along-track and across-track derivatives were smoothed with a 32-point (480-m) boxcar and the vertical derivative was smoothed with a 200-point (3000-m) boxcar averager to reduce the high-frequency noise. Because the horizontal derivative measurements were much less noisy than the vertical derivative measurements, the former were gridded and used to calculate g_{VV} via equation (B26). Equations (B13)-(B21) were then used to calculate the

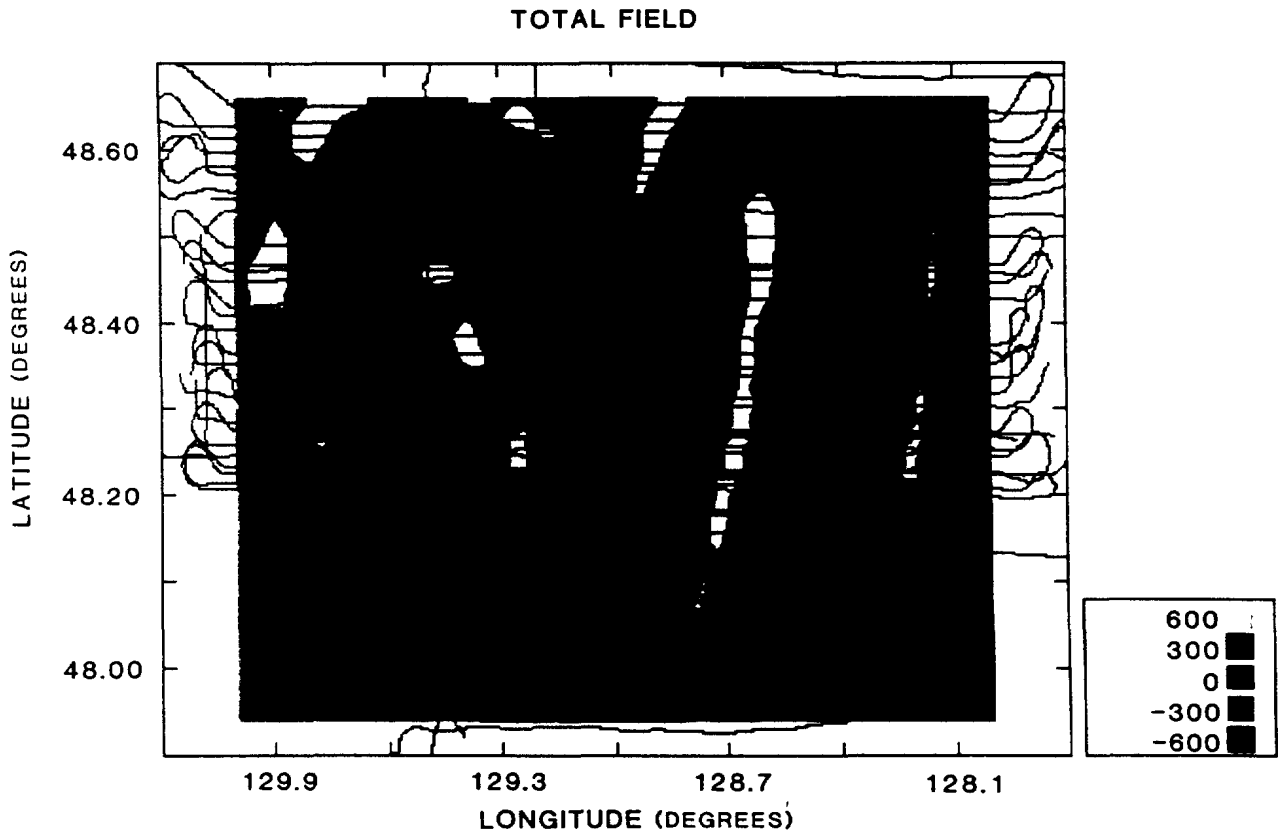


Figure 1. Total-field over entire area, showing aircraft lines. (Altitude is 300 m, units are nT.)

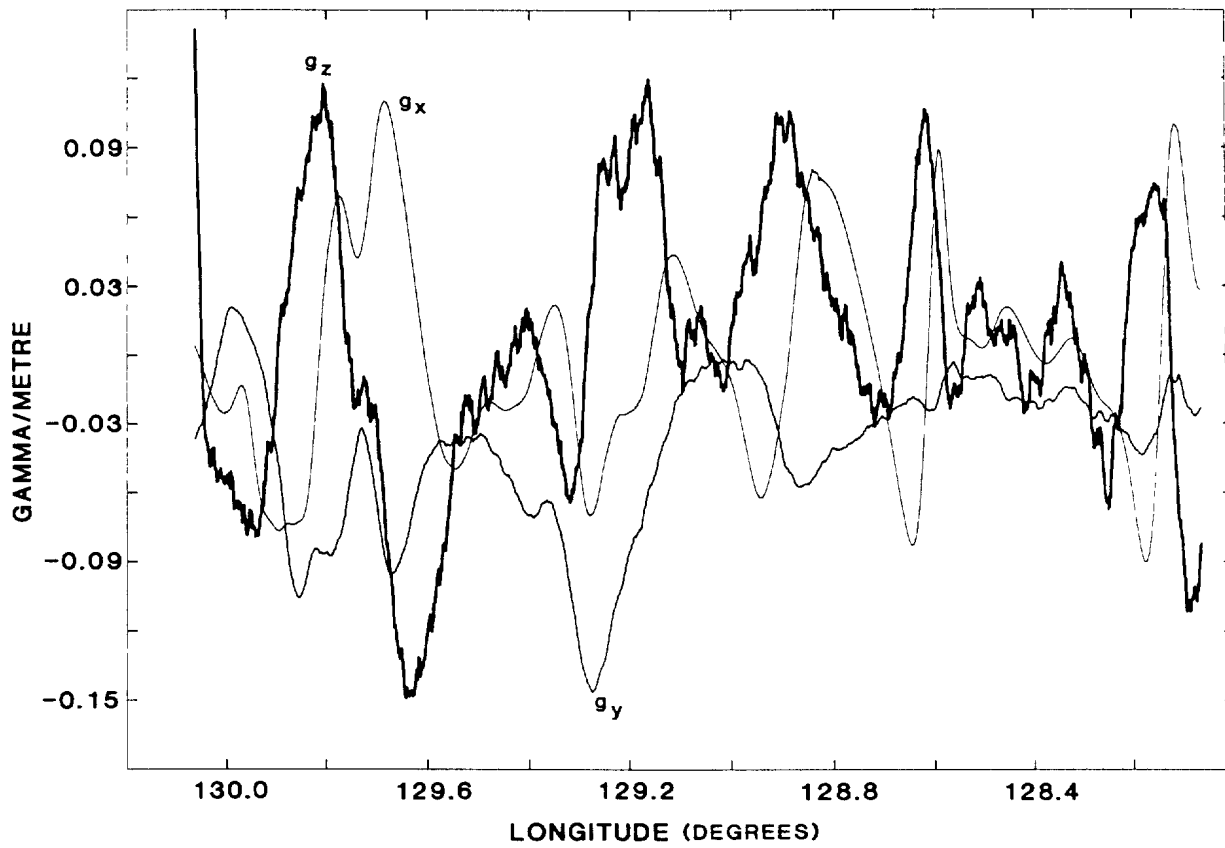


Figure 2. Along-track, across-track and vertical derivative measurements along a single profile.

remaining tensor components. Note the subscript "n" refers to "north", "e" to "east", and "v" to "vertically down".

Figures 3(a,b)-7(a,b) are colour-fill contour plots of the tensor components g_{nn} , g_{ne} , g_{nv} , g_{ev} and g_{vv} computed from the gridded horizontal derivatives. The units are nT/m. All plots correspond to a flight altitude of 300 m above sea-level. Figures 8(a,b)-12(a,b) are surface grid plots of the same information, although the grid has been subsampled by a factor of 5 for ease of plotting.

Canadian Hydrographic Office bathymetric maps were digitized and gridded at the same sampling interval as the magnetic data (see Figure 13, units are metres). The gridded total-field data from each area were multiplied by a two-dimensional sine taper window to reduce the effects of spectral leakage. These two data sets were then combined via equation (C12) to estimate the magnetization for a 500 m thick layer of magnetized material following the topography of the sea-floor in each area. The signal due to a single prism (148 m \times 222 m \times 500 m), at a depth of 2800 m, and magnetized parallel to the Earth's field, was computed numerically on the same size grid as was used for the magnetic and bathymetric measurements. The Fourier transform of these were then computed numerically to generate "FFT(S)" used in equation (C12). The summation in equation (C12) was cut off at only the first term (involving the first derivative), and only one iteration was used (M_1). Figure 14 is a colour-fill contour map of the calculated magnetization for regions A and B. The magnetization units are nT (cgs units of susceptibility \times average value of the Earth's magnetic field).

Two points should be made regarding the accuracy of the magnetization estimate. Boundary effects are quite noticeable around the perimeter of the grid and are responsible for the apparent discontinuity between the upper and lower regions. These are artifacts of the windowing and digital Fourier transform and should not be considered real features. As well, anomalies tend to be "broken up" in the north-south direction, more so than in the east-west direction. This is due to the oscillation introduced by the gridding routine becoming even more pronounced in the deconvolution process.

Several magnetization features are quite distinct and should be noted. The approximately north-south lineations are due to sea-floor spreading, with the central anomaly (overlying the spreading centre) lying near

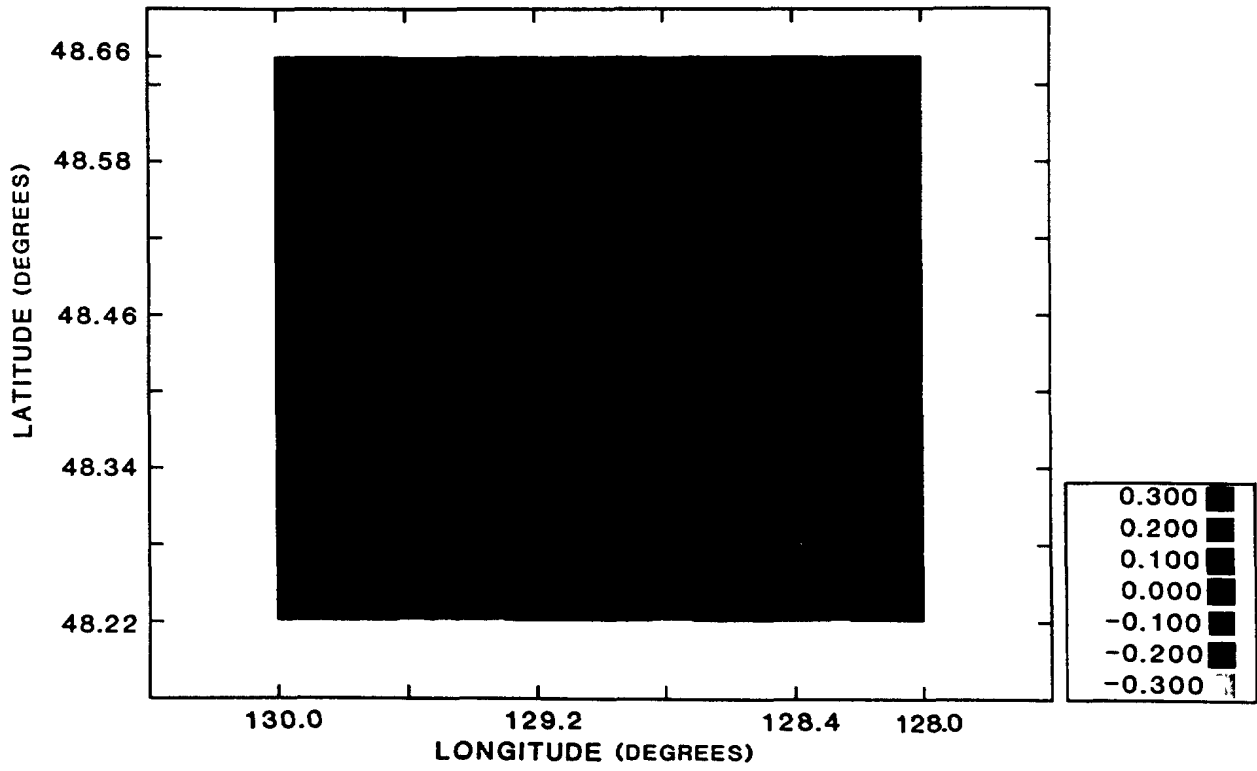


Figure 3(a). Contour plot of g_{nn} over region A (300 m, units are nT/m).

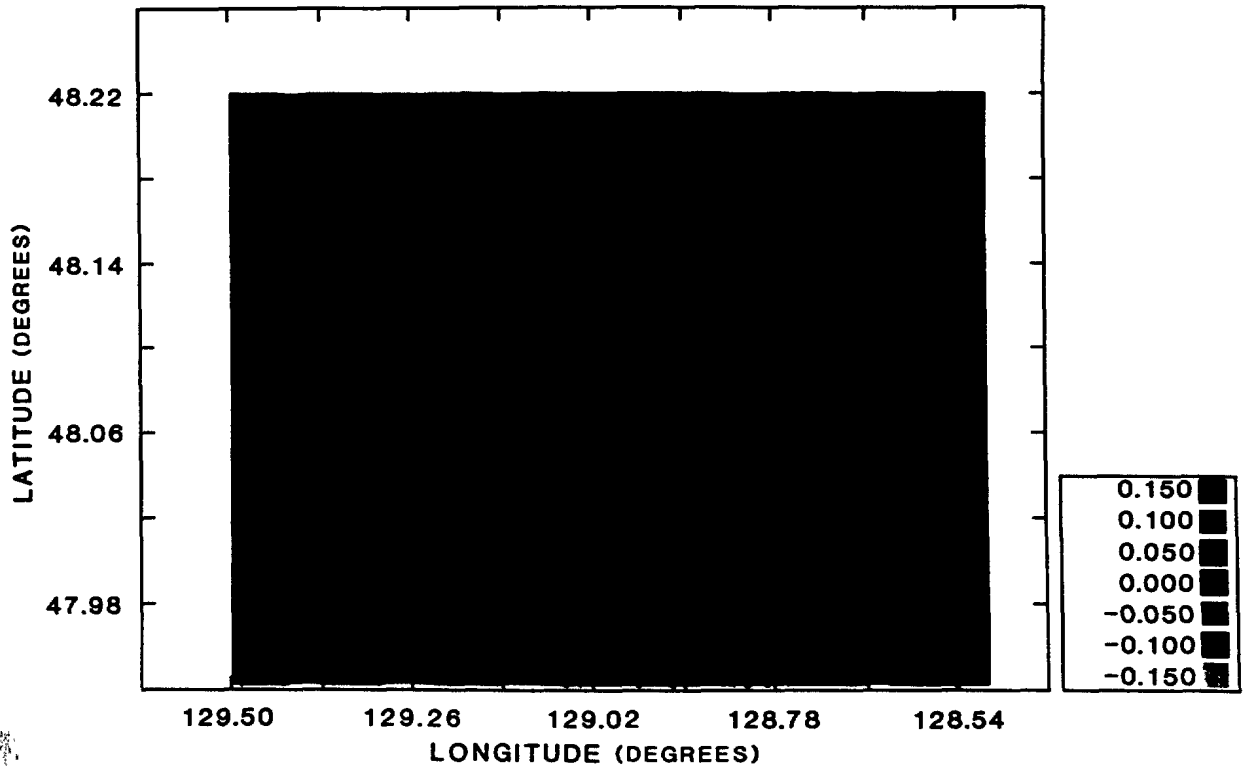


Figure 3(b). Contour plot of g_{nn} over region B (300 m, units are nT/m).

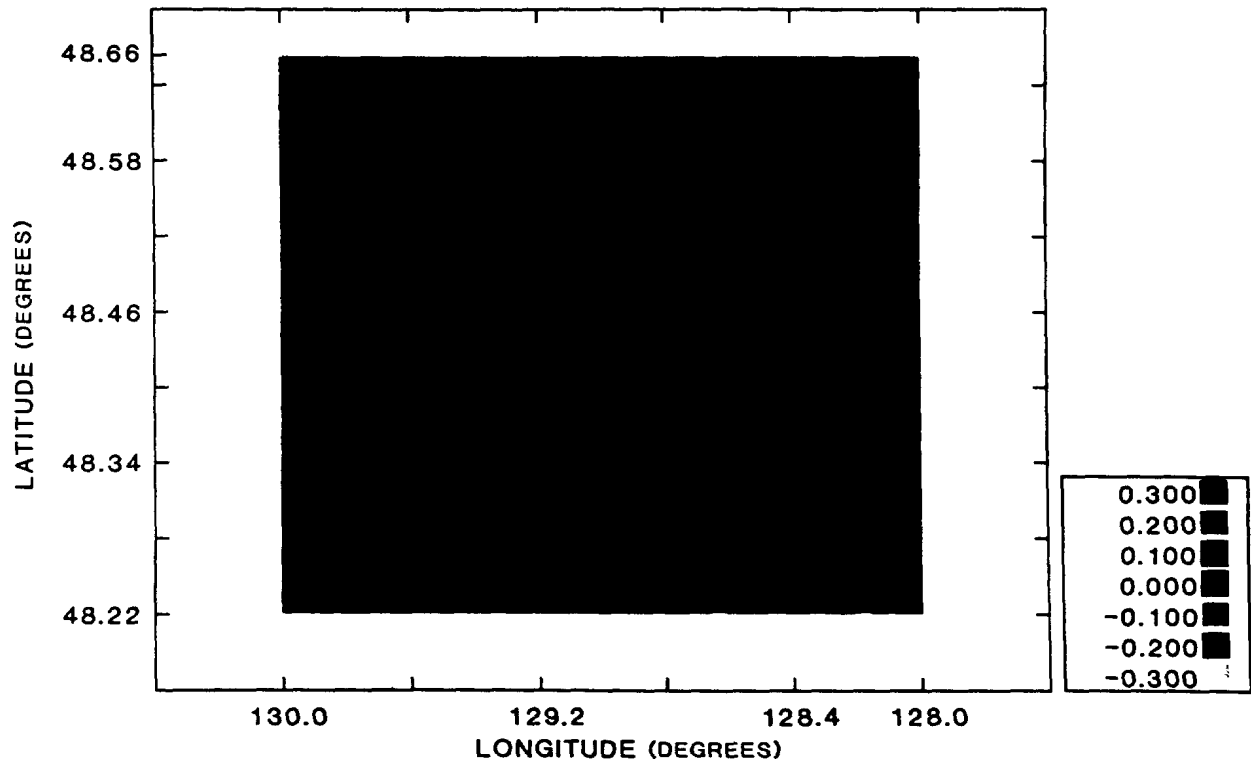


Figure 4(a). Contour plot of g_{ne} over region A (300 m, units are nT/m).

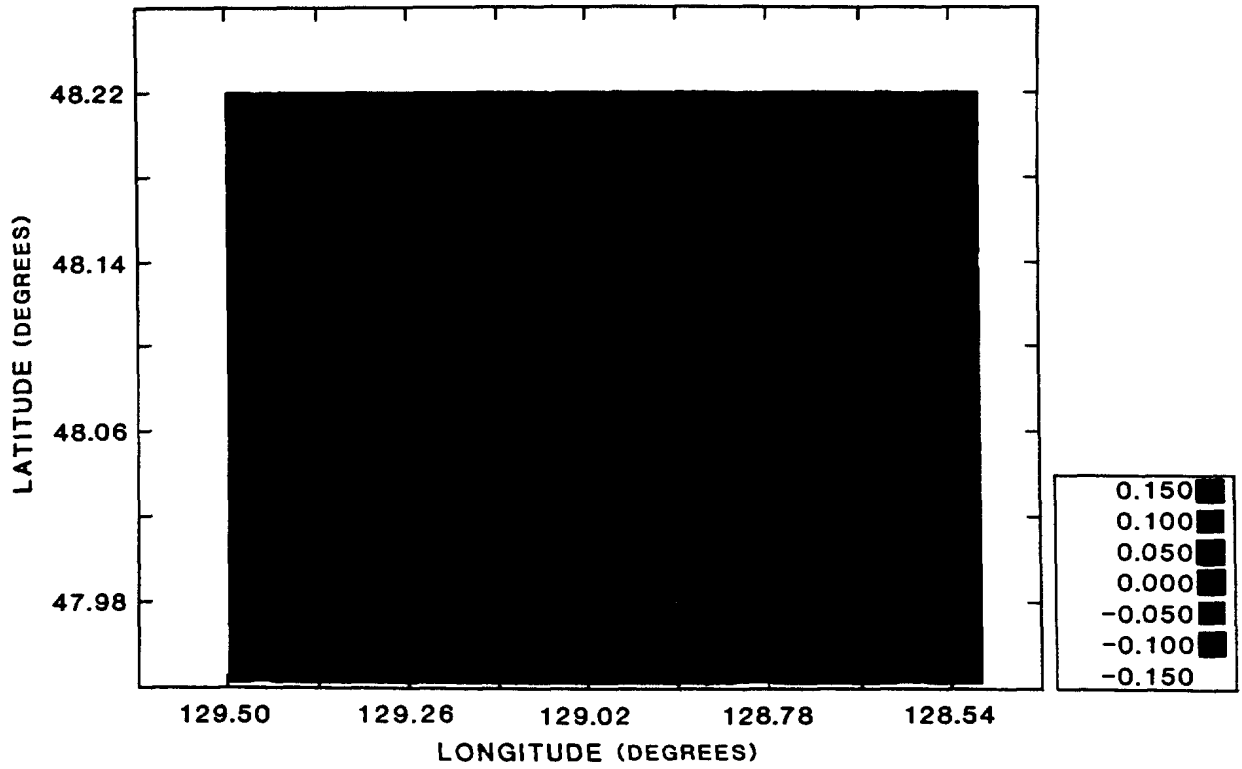


Figure 4(b). Contour plot of g_{ne} over region B (300 m, units are nT/m).

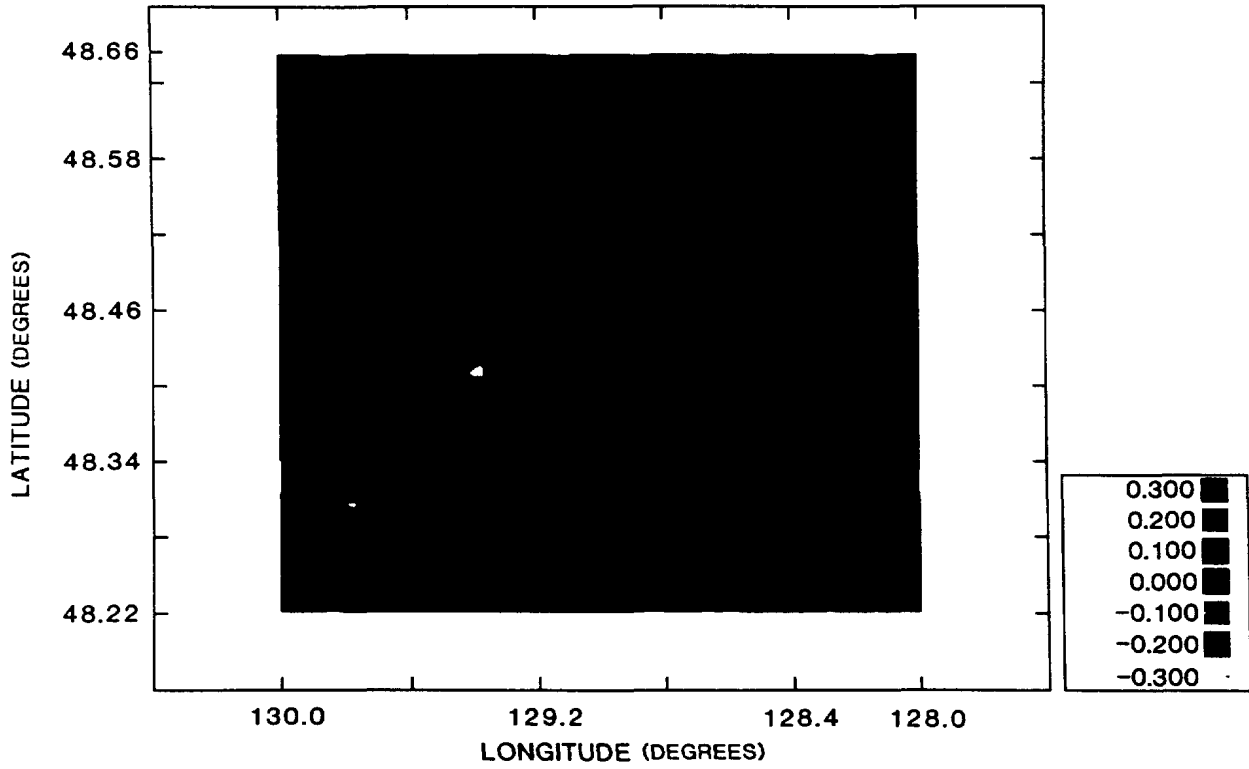


Figure 5(a). Contour plot of g_{NV} over region A (300 m, units are nT/m).

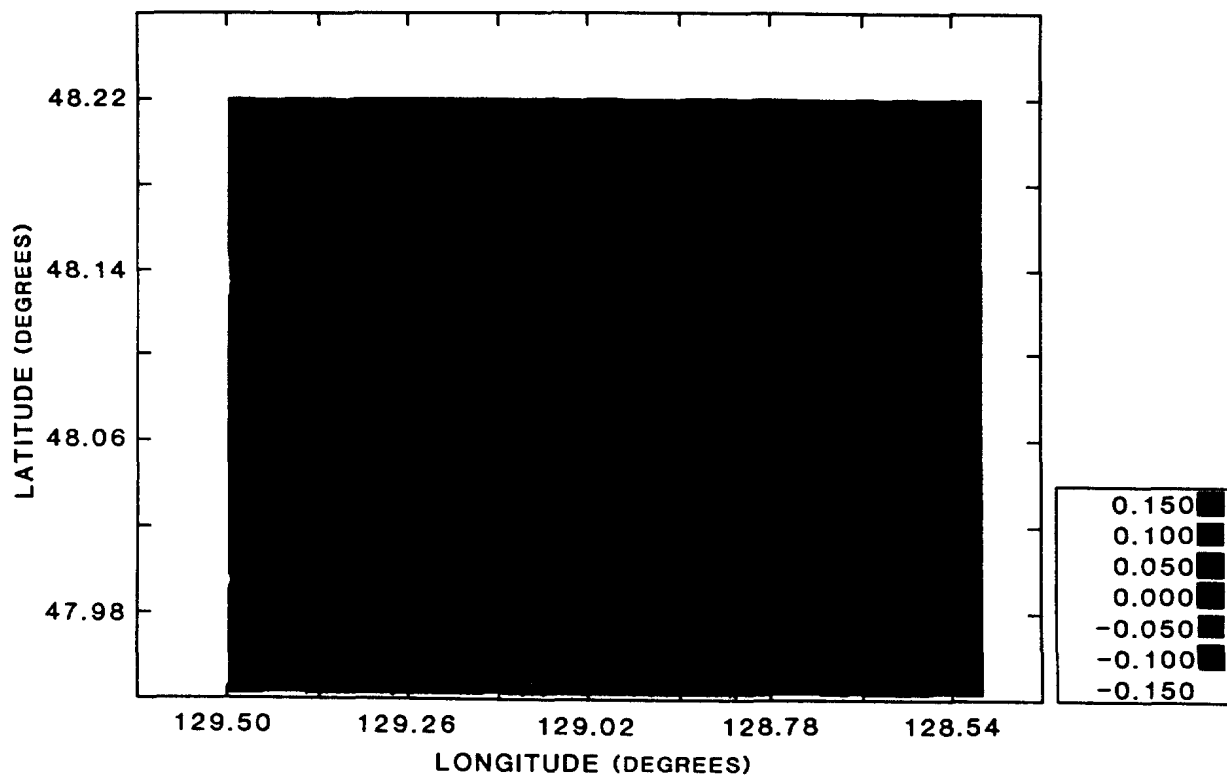


Figure 5(b). Contour plot of g_{NV} over region B (300 m, units are nT/m).

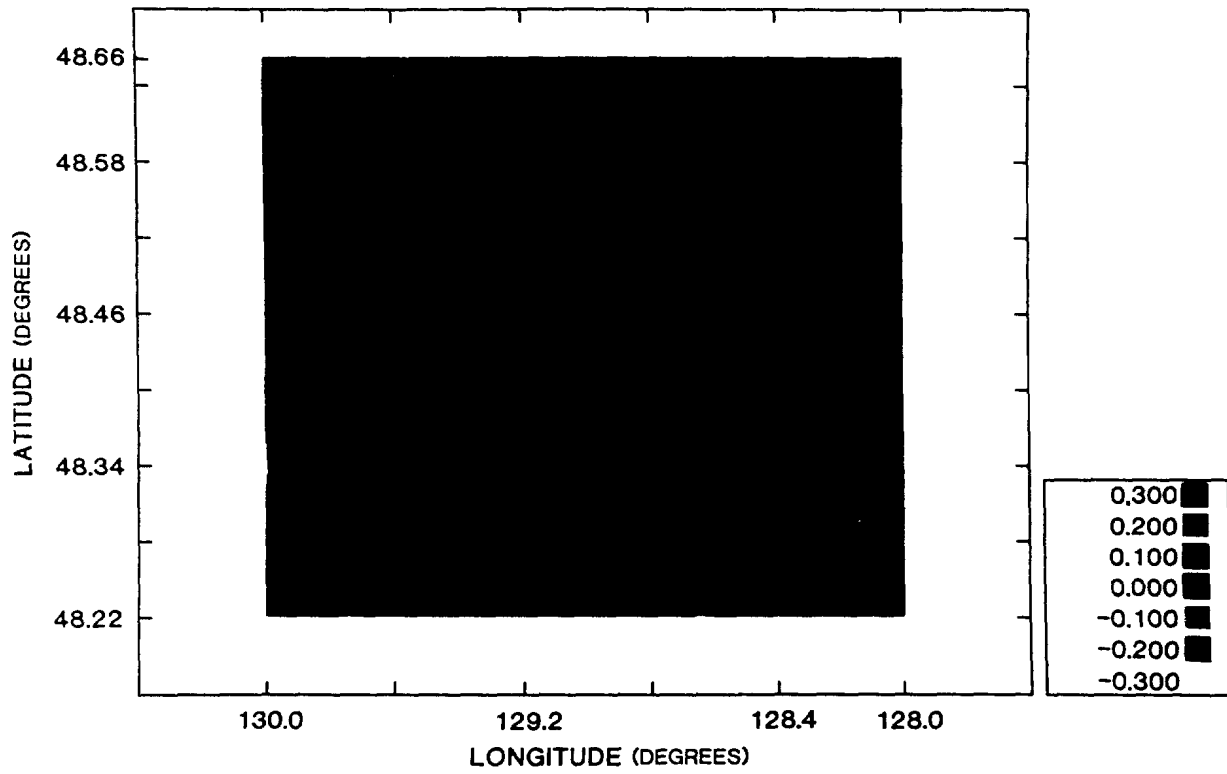


Figure 6(a). Contour plot of g_{EV} over region A (300 m, units are nT/m).

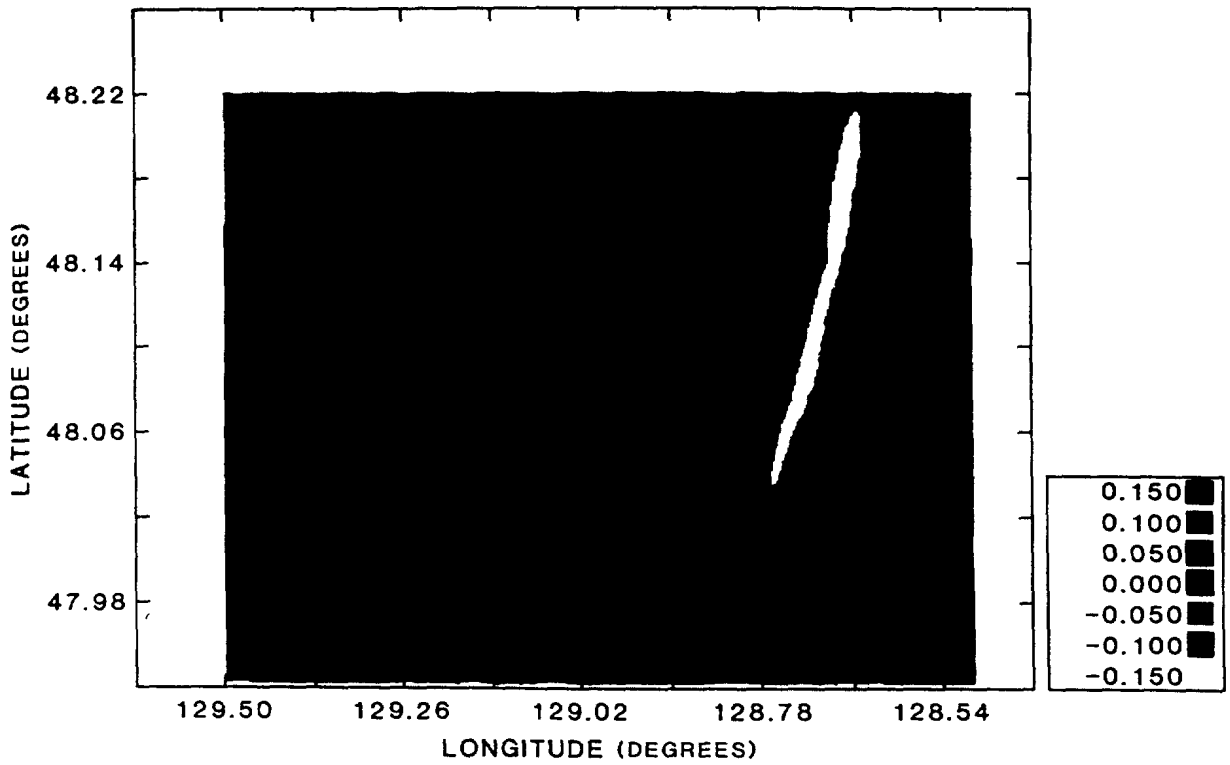


Figure 6(b). Contour plot of g_{ev} over region B (300 m, units are nT/m).

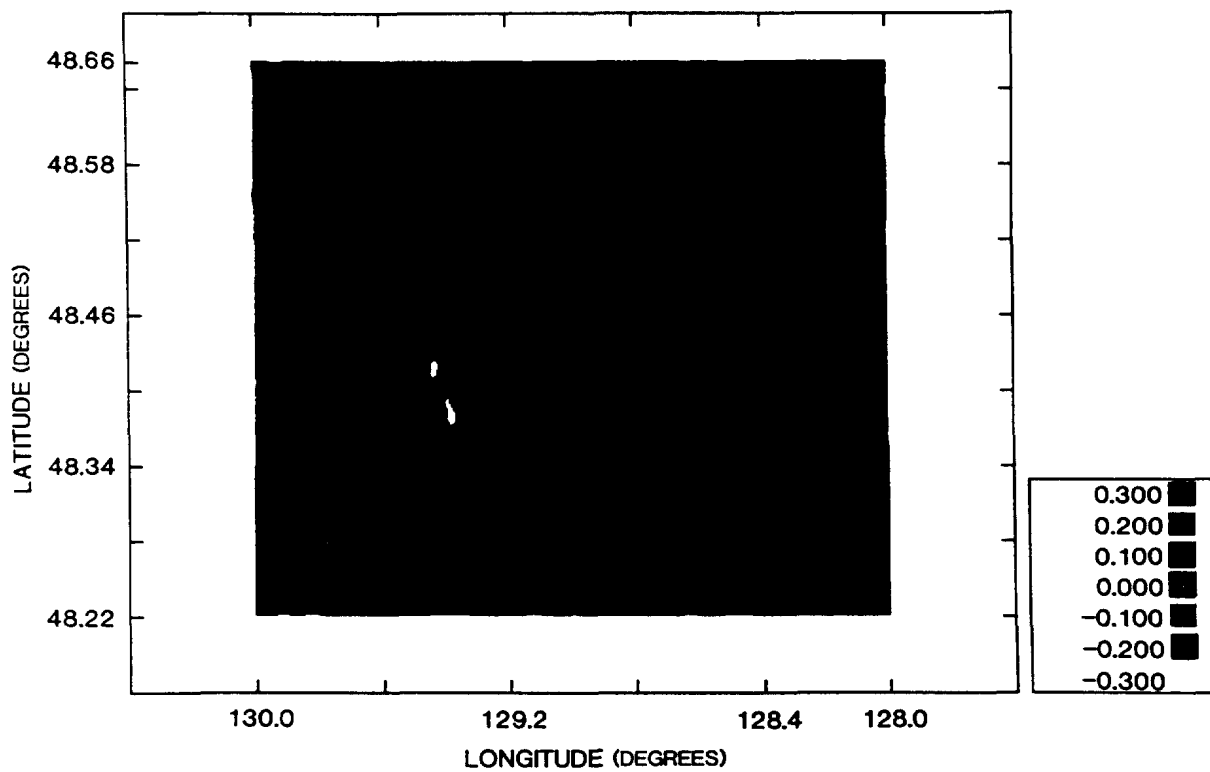


Figure 7(a). Contour plot of g_{VV} over region A (300 m, units are nT/m).

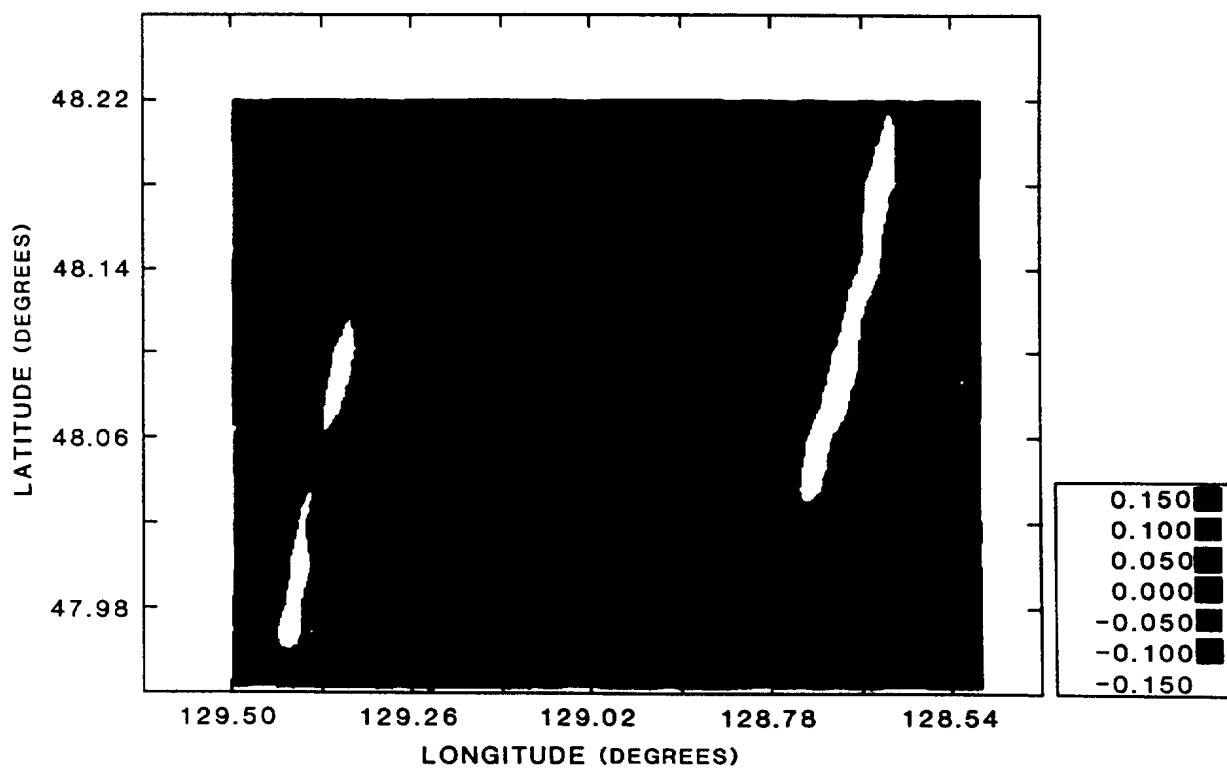


Figure 7(b). Contour plot of g_{VV} over region B (300 m, units are nT/m).

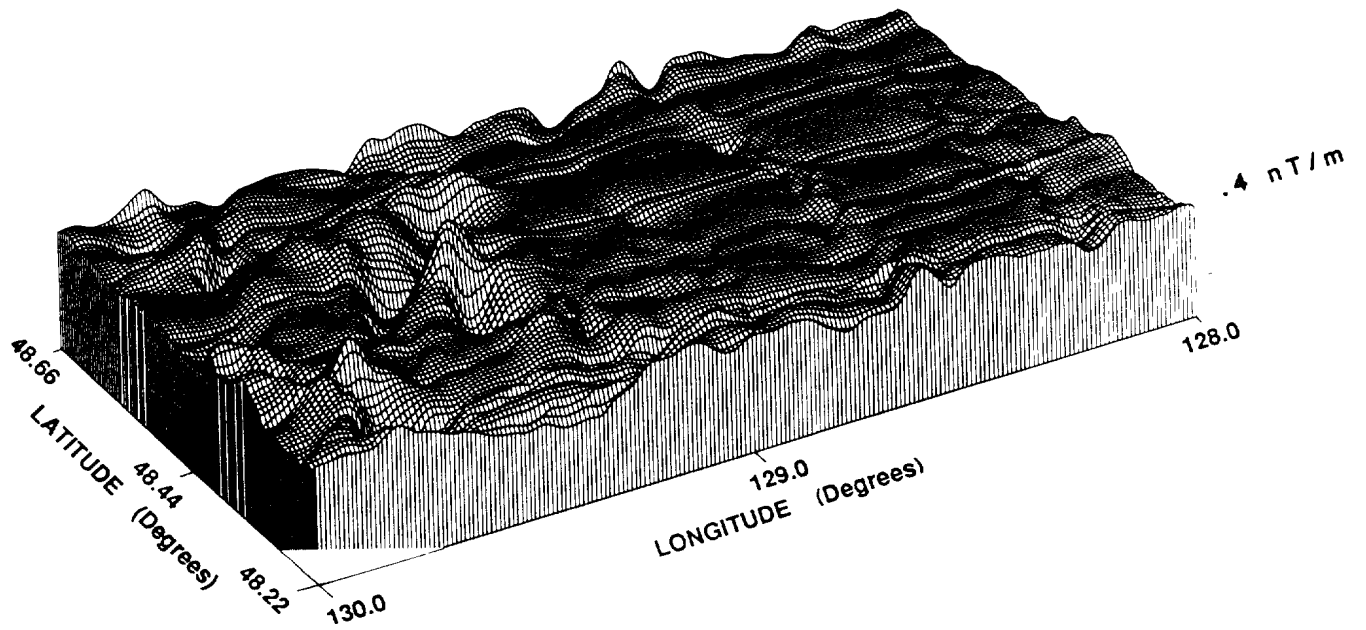


Figure 8(a). Surface grid plot of g_{nn} over region A (300 m).

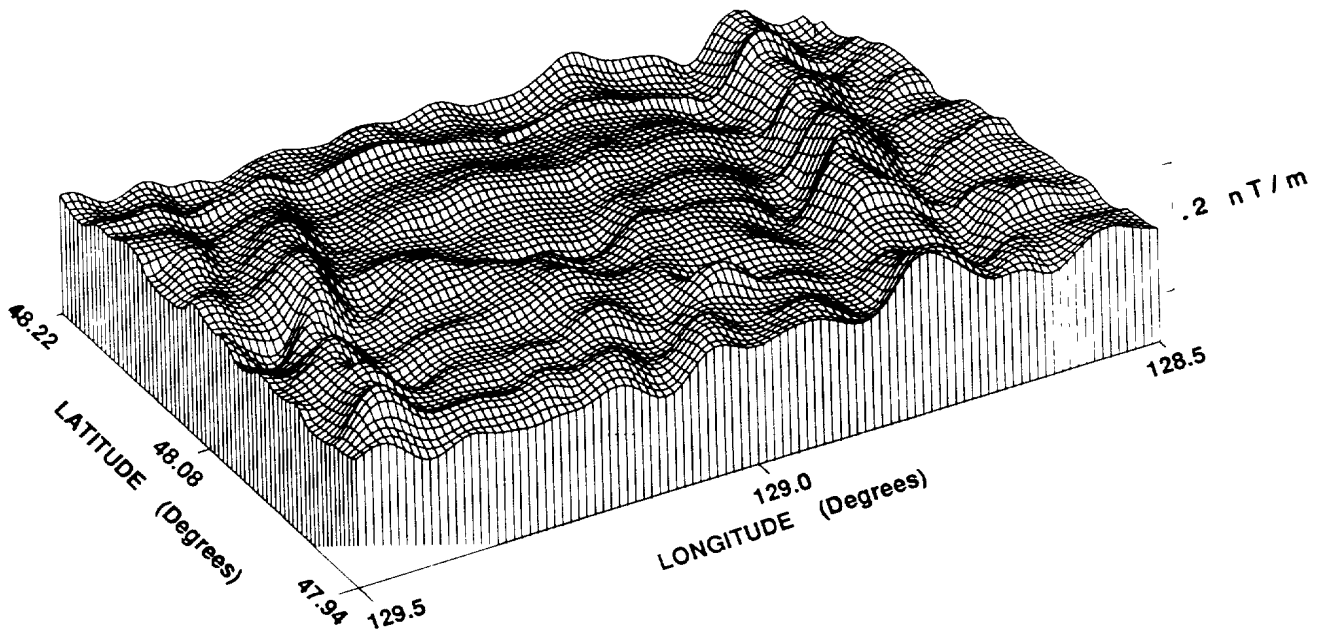


Figure 8(b). Surface grid plot of g_{nn} over region B (300 m).

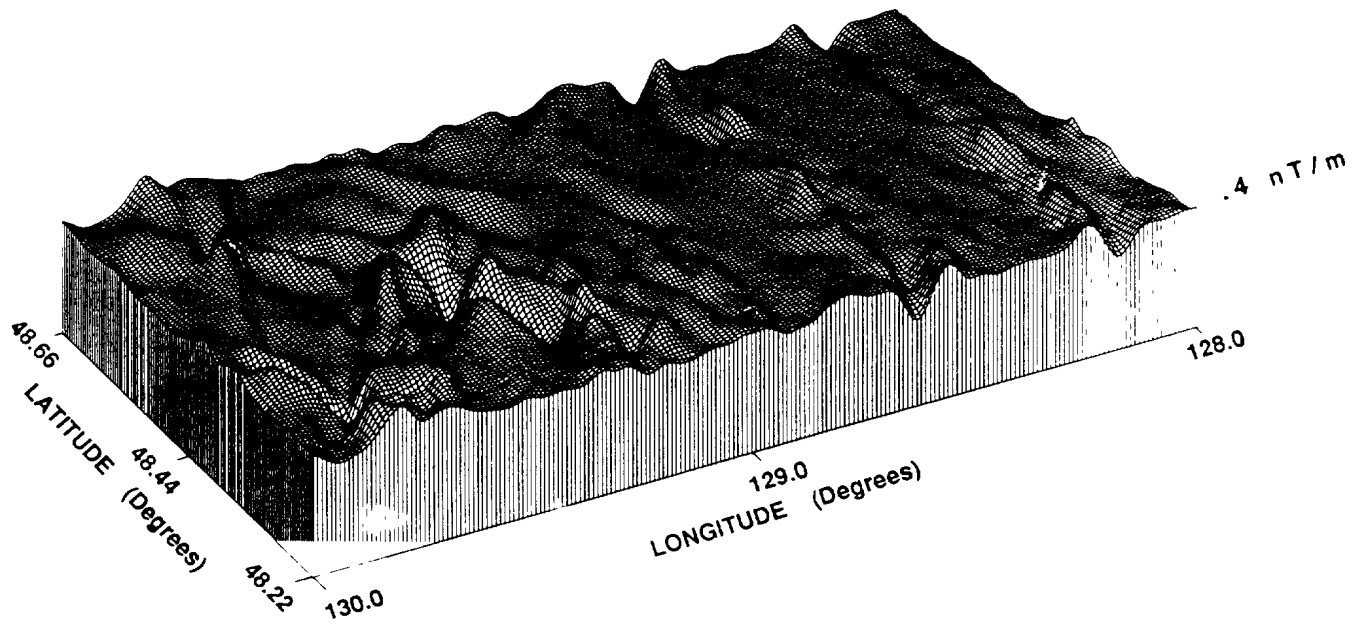


Figure 9(a). Surface grid plot of g_{ne} over region A (300 m).

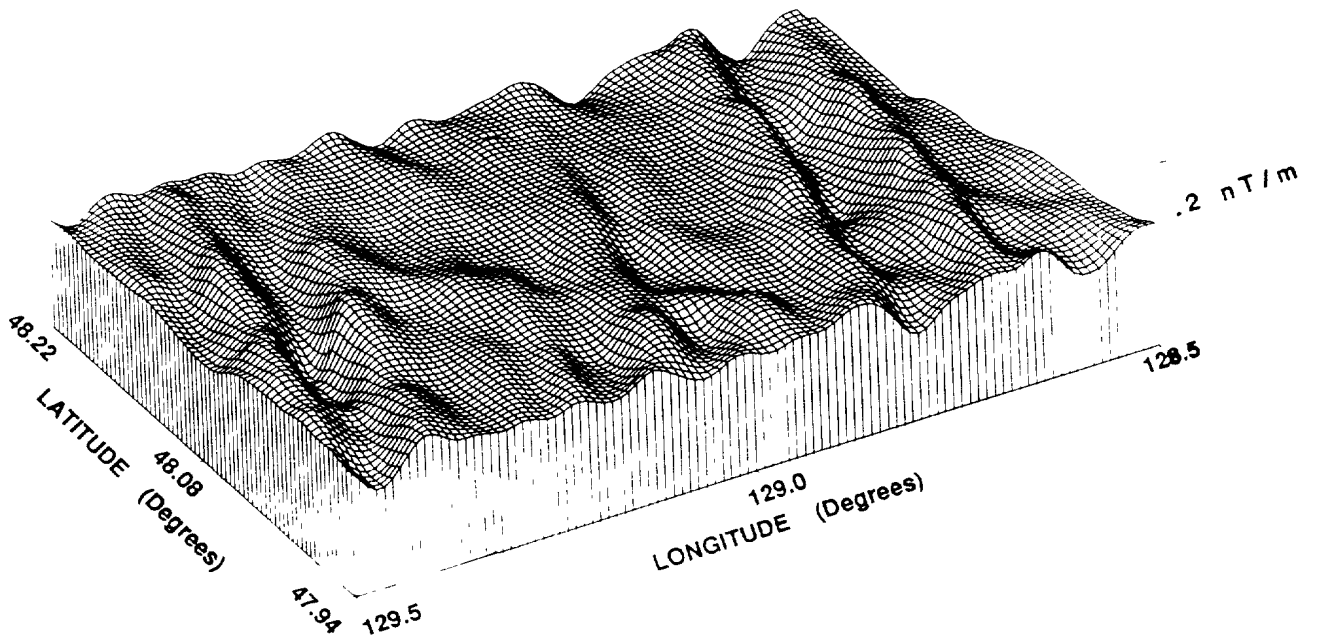


Figure 9(b). Surface grid plot of g_{ne} over region B (300 m).

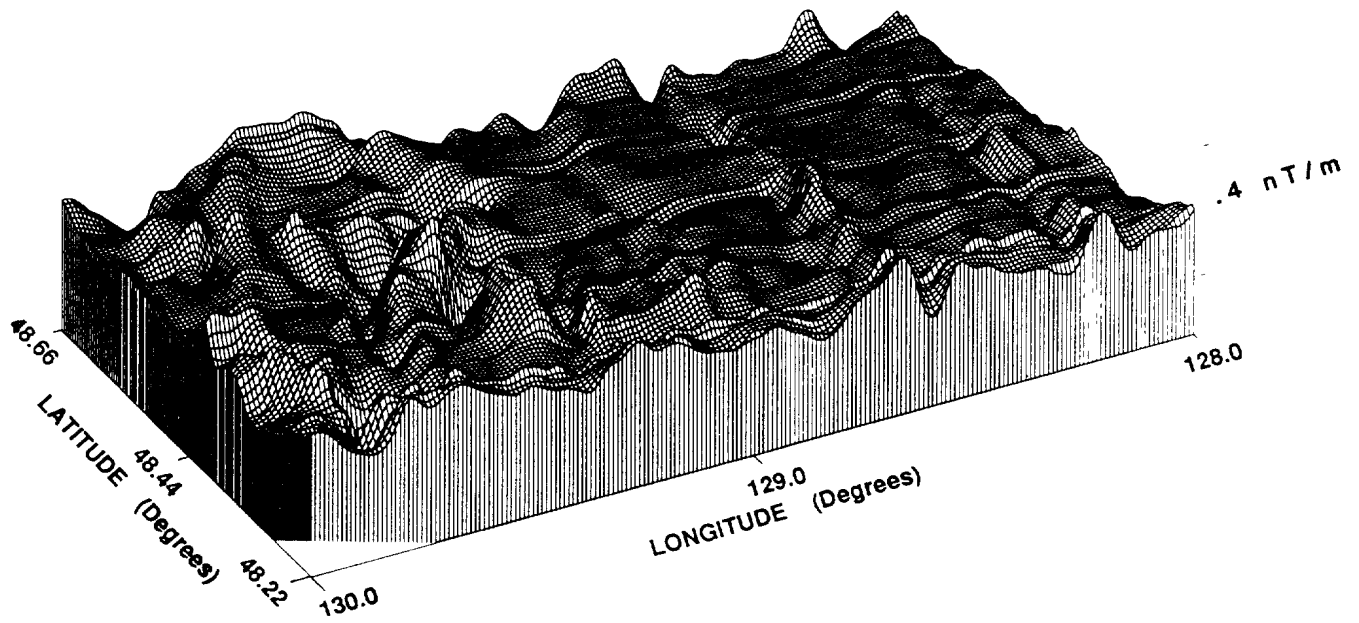


Figure 10(a). Surface grid plot of g_{NV} over region A (300 m).

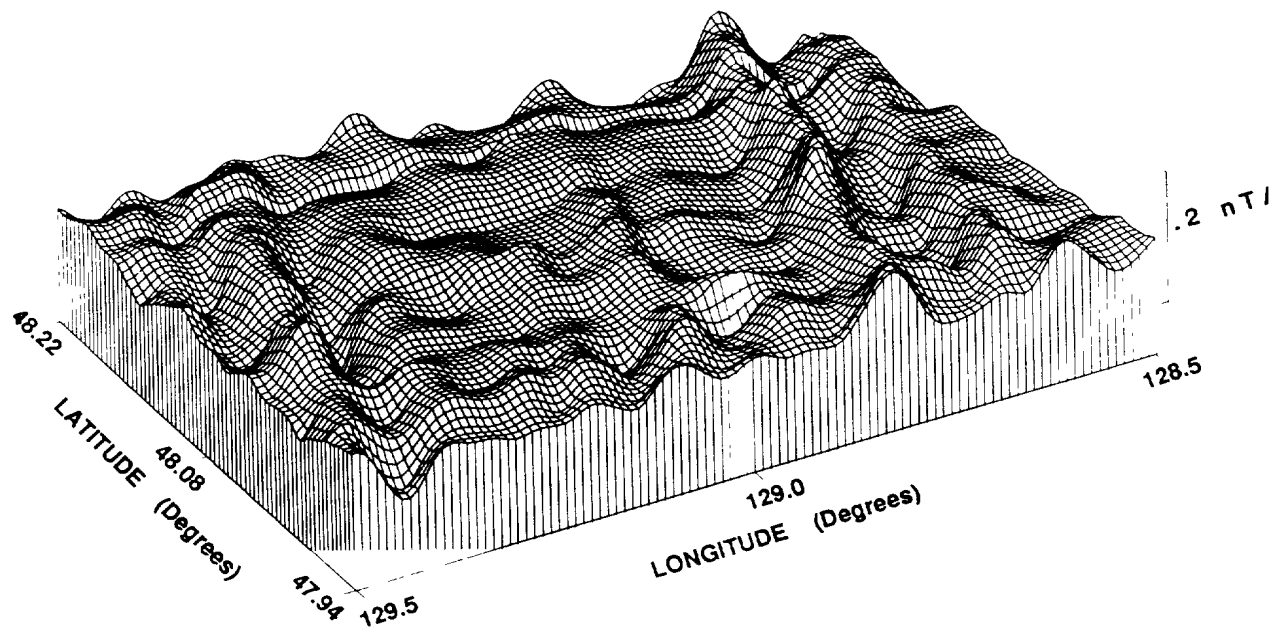


Figure 10(b). Surface grid plot of g_{NV} over region B (300 m).

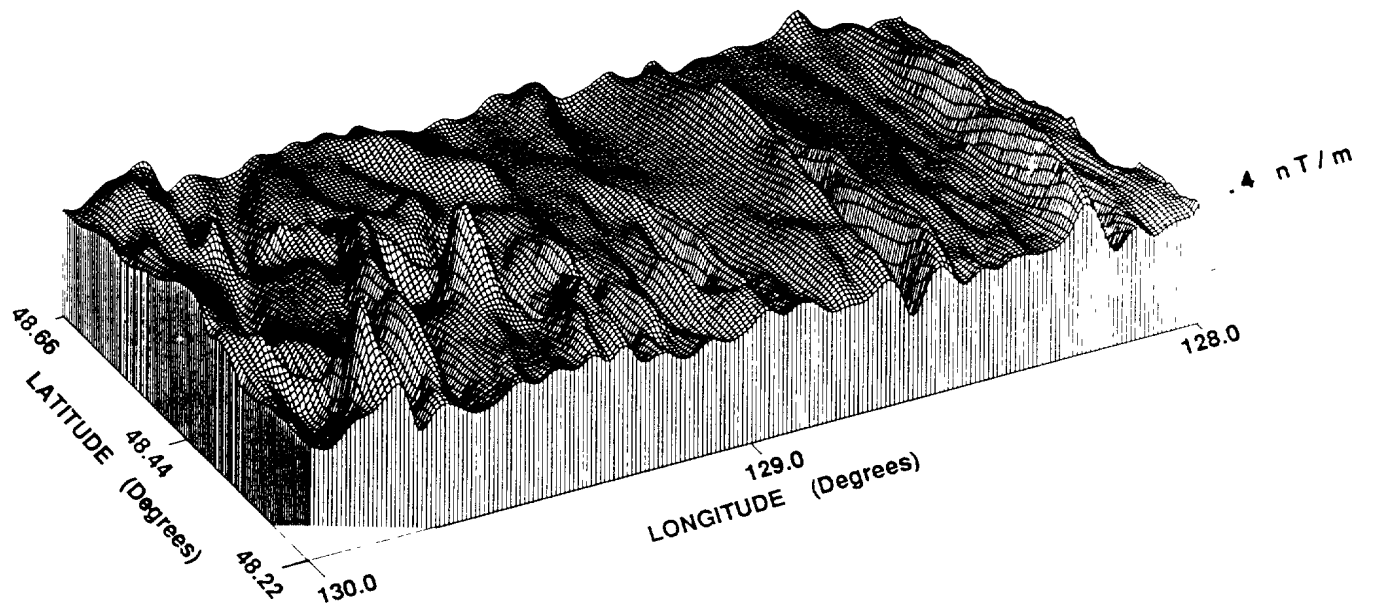


Figure 11(a). Surface grid plot of g_{eV} over region A (300 m).

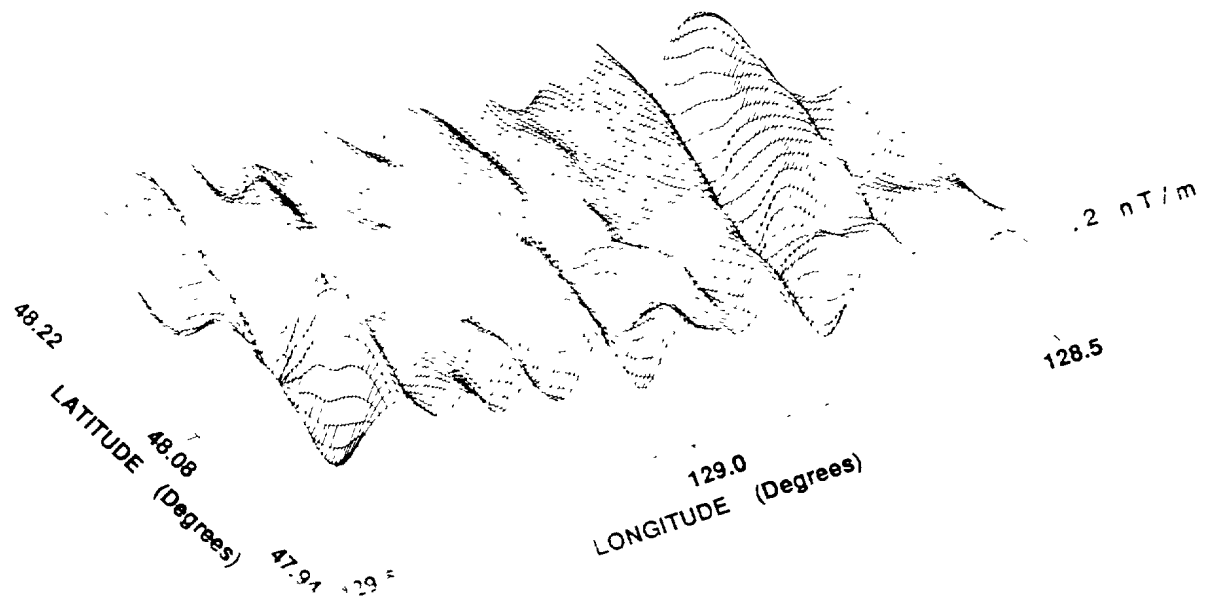


Figure 11(b). Surface grid plot of g_{ev} over region B (300 m).

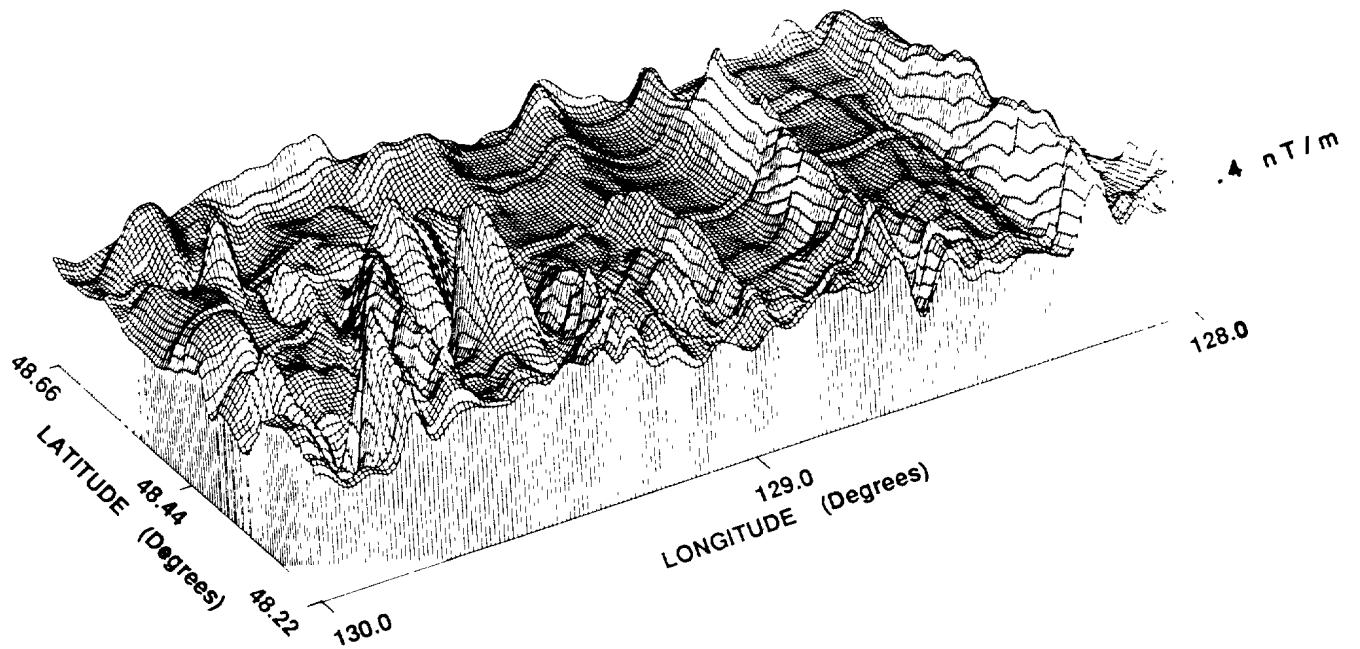


Figure 12(a). Surface grid plot of g_{VV} over region A (300 m).

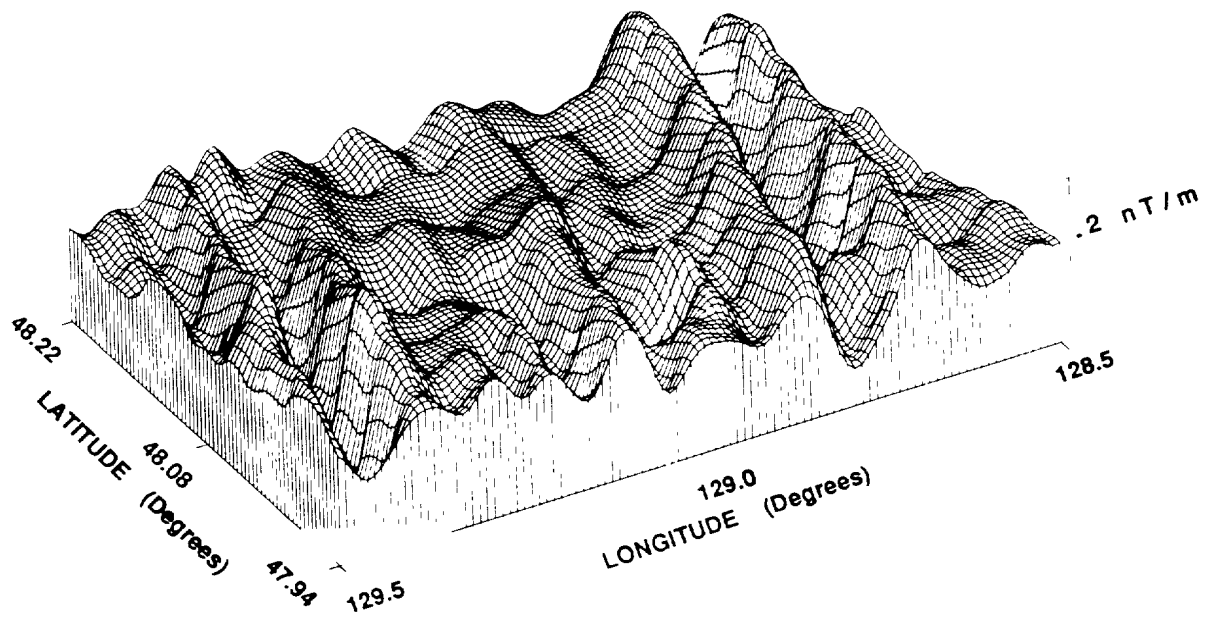


Figure 12(b). Surface grid plot of g_{VV} over region B (300 m).

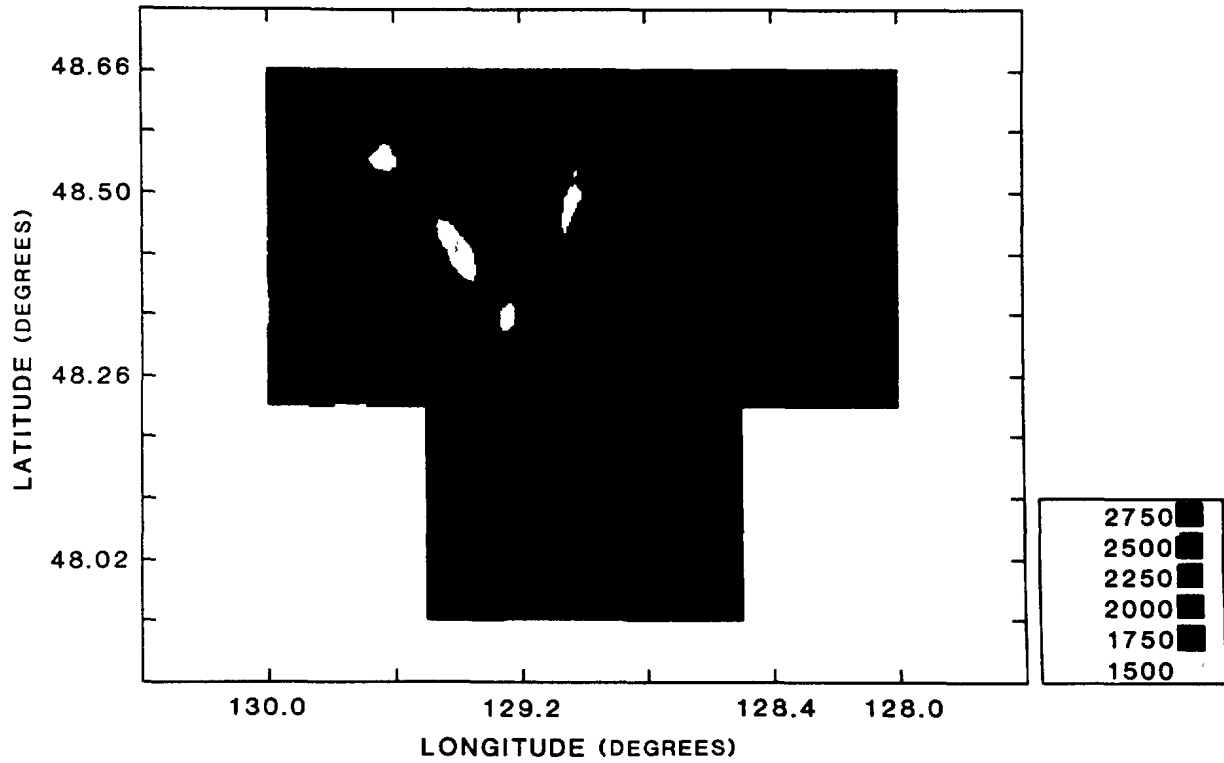


Figure 13. Bathymetric contour plot of entire area (units are m).

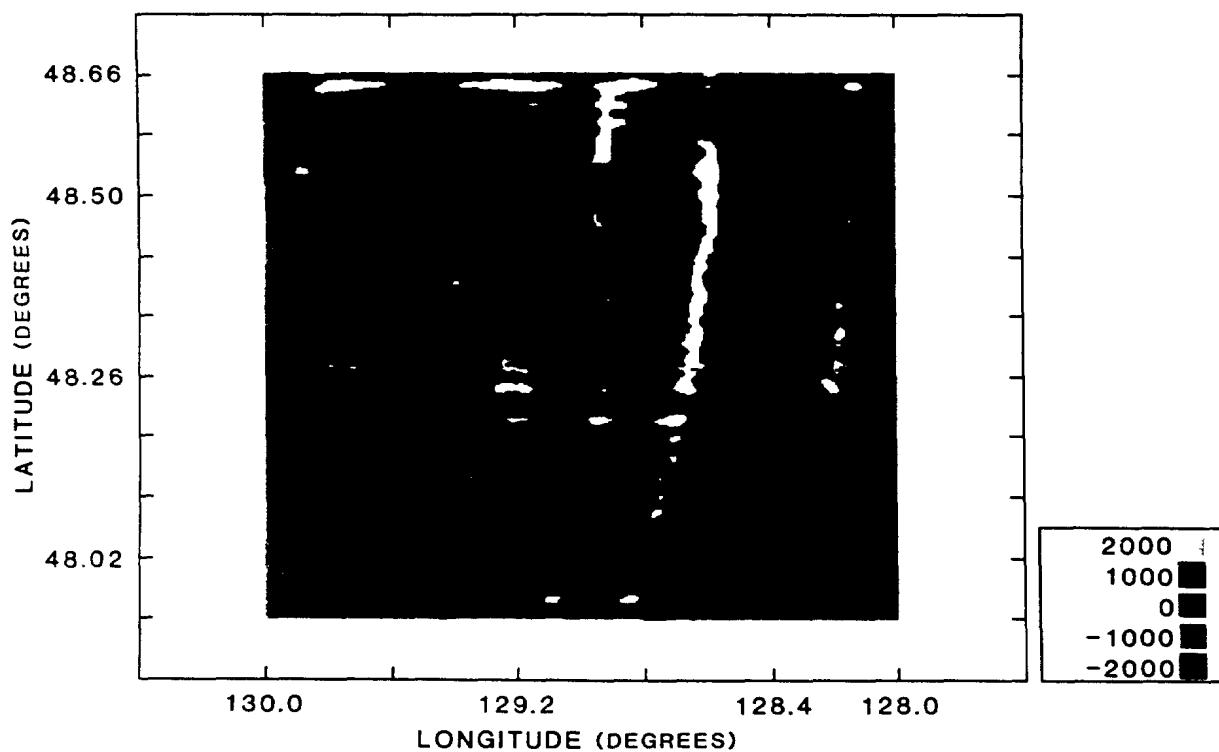


Figure 14. Magnetization estimate for entire area (units are nT).

longitude 129.0°W. The sharp boundary between positive and negative magnetization along 128.6°W corresponds to the Brunhes-Matuyama reversal (.69 million years before present), and the sharp positive anomaly along 128.2°W is the Gilsa event (1.63 to 1.79 mybp). While the corresponding features are present on the opposite side of the spreading centre, their amplitudes appear to be reduced. The reason for this asymmetry is not known.

There is a small region along the Brunhes-Matuyama boundary where the magnetization is very strongly positive (48.52°N, 128.6°W). This is not an artifact of the gridding or inversion algorithms as there is almost a 200 nT anomaly present in the raw total-field data. Similarly, it is probably not due to incorrect depth-to-source information because if the magnetic layer lies beneath the measured bathymetry, then the anomaly would be smaller, not larger than the adjacent anomaly. Also, it is unlikely that the bathymetric data is missing what would have to be a sharp rise of several hundred metres to account for this total-field anomaly. Finally, there is no evidence that the remainder of the Brunhes-Matuyama boundary has more sediment cover than this small region (McManus et al., 1972).

There appears to be a general reduction in the magnetization north of 48.26°N at 128.9°W, within the Brunhes-aged crust. This area, named Middle Valley, is overlain with a deep blanket of sediment and is an area of hydrothermal activity. It is thought that this sedimentary layer reduces the interaction between hydrothermal fluids and the surrounding seawater, causing more leaching of the iron oxides from the basalt than would occur if there were no sedimentary layer. This removes magnetic material, leaving a region which has a lower bulk magnetization (Levi and Riddihough, 1986).

Finally, the sea-mounts appear to have some slight magnetization anomalies associated with them, although this may just be a mismatch between the filtering applied to the bathymetric data by the Canadian Hydrographic Service, and the filtering applied to these magnetic data.

Figure 15 is a two-dimensional power spectrum of the total-field at an altitude of 300 m above sea-level over region A. The axes have been converted from wavenumber to Hz by assuming an aircraft speed of 100 m/s.

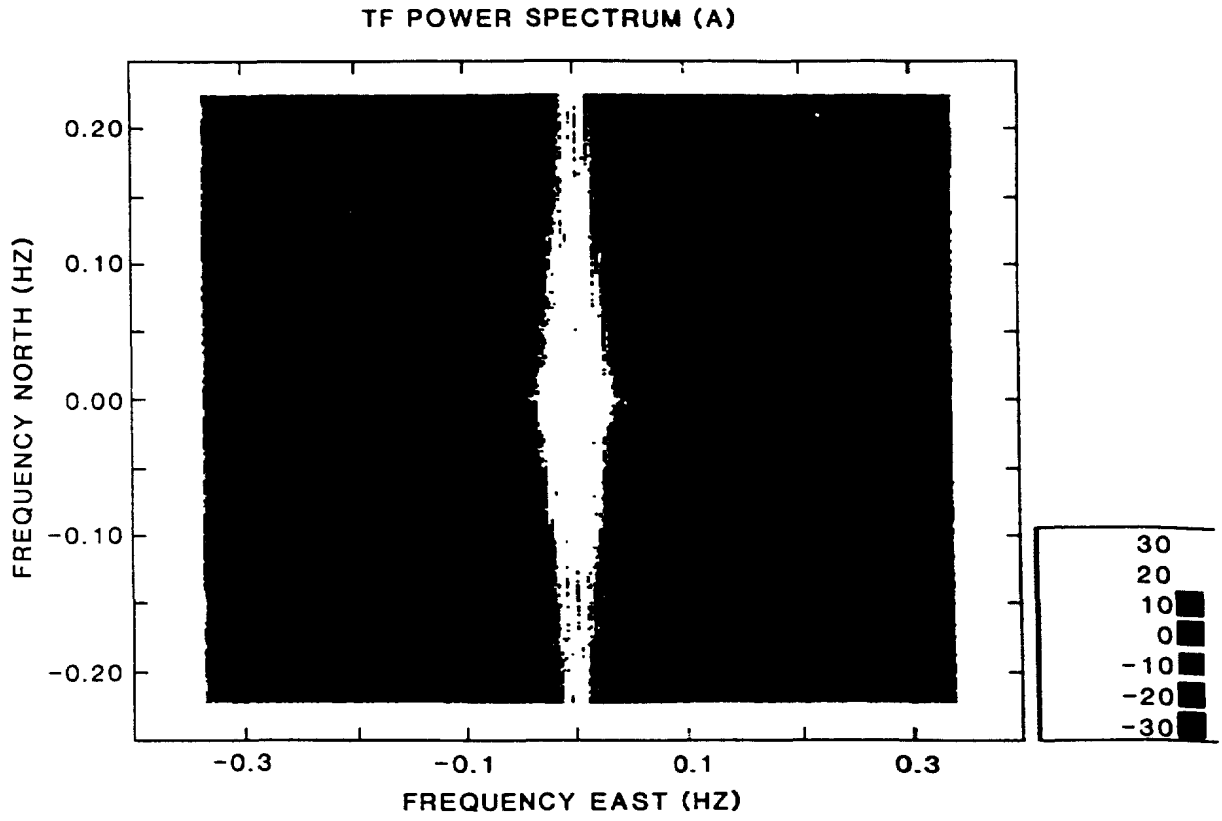


Figure 15. Contour plot of the power spectrum of total-field measurements over Region A (units are dB relative to arbitrary units).

The spectrum appears to be elongated along the north axis but this is probably due to the sparse sampling in this direction and the oscillation problems in the gridding routine. Most of the power along the east axis lies at very low frequencies (<0.05 Hz), but there is still significant power even out to 0.1 Hz. (The power at frequencies above 0.1 Hz is probably due to aircraft miscompensation and micropulsation activity, not geological noise.) Recall that there is very little information at wavelengths less than 2 km in Geological Survey of Canada magnetic contour maps. For aircraft speeds of 100 m/s, this means that they contain very little information at frequencies above 0.05 Hz. Figure 15 clearly illustrates that simply digitizing GSC maps will not give sufficiently accurate geological noise models for all MAD simulations.

4. CONCLUSIONS

Gradient tensor component maps for an altitude of 300 m above sea-level have been generated from measurements of the horizontal derivative of the total-field over the northern end of the Juan de Fuca Ridge. They are digitized with a sampling interval of 148 m in the east direction and 222 m in the north direction. These maps contain geological information at higher frequencies than is possible by digitizing GSC magnetic contour maps.

As well, a model of the underlying magnetization has been developed from the total-field measurements. This model, when combined with bathymetric measurements of the area, may be used to calculate the total-field, its derivatives, and the tensor gradient components anywhere above the modelled area. The magnetization and bathymetry models are digitized at the same interval as the tensor component maps.

Computer simulations of airborne MAD systems are being developed at DREP. These simulations require accurate models for the geological noise contribution to the magnetometer output. This geological noise can be modelled in either the space or the wavenumber domain, but the latter is probably more efficient for computer simulations. This is because the models can be most easily adapted to slightly different conditions (change

of altitude, or change of spatial sampling rate) in the wavenumber domain. In addition, new geological environments can be modelled very easily with the Juan de Fuca magnetization and different bathymetry data. These new models are most easily developed in the wavenumber domain.

5. REFERENCES

Atwater, T., and Mudie, J., 1973; Detailed near-bottom geophysical study of the Gorda Rise, Jour. Geophys. Res., 78, 8665-8686.

Henderson, R.G., 1970; On the validity of the use of the upward-continuation integral for total magnetic intensity data, Geophysics, 35, 916-919.

Henderson, R.G., and Zeitz, I., 1949; The upward-continuation of anomalies in total magnetic intensity fields, Geophysics, 14, 517-534.

Klitgord, K.D., Huestis, S.P., Mudie, J., and Parker R.L, 1975; An analysis of near-bottom magnetic anomalies: sea-floor spreading and the magnetized layer, Geophys. J. R. Ast. Soc., 43, 387-424.

Levi, S., and Riddihough, R., 1986; Why are marine magnetic anomalies suppressed over sedimented spreading centers?, Geology, 14, 651-654.

McManus, D.A., Holmes, M.L., Carson, B., and Barr, S.M., 1972; Late quaternary tectonics, northern end of Juan de Fuca Ridge (Northeast Pacific), Marine Geology, 12, 141-164.

Nabighian, M.N., 1984; Toward a three-dimensional automatic interpretation of potential field data via generalized Hilbert transforms: Fundamental relations, Geophysics, 49, 780-786.

Nelson, J. Bradley, 1986; An alternate derivation of the three-dimensional Hilbert transform relations from first principles, Geophysics, 51, 1014-1015.

Nelson, J. Bradley, 1988; Calculation of the magnetic gradient tensor from total-field gradient measurements and its application to geophysical interpretation, Geophysics, 53, 957-966.

Parker, R.L., 1972; The rapid calculation of potential anomalies, Geophys. J. R. Ast. Soc., 31, 447-455.

Parker, R.L., and Huestis, S.P., 1974; The inversion of magnetic anomalies in the presence of topography, J. Geophys. Res., 79, 1587-1593.

Schouten, H., and McCamy, K., 1972; Filtering marine magnetic anomalies, J. Geophys. Res. 77, 7089-7099.

6. APPENDICES

- A: INTEGRAL RELATIONS BETWEEN TENSOR GRADIENT COMPONENTS
- B: RELATIONS BETWEEN THE TOTAL-FIELD, THE TOTAL-FIELD
DERIVATIVES, AND THE GRADIENT TENSOR: FREQUENCY DOMAIN
- C: CALCULATION OF THE MAGNETIZATION

APPENDIX A

INTEGRAL RELATIONS BETWEEN TENSOR GRADIENT COMPONENTS

These relationships have been investigated previously by Nelson (1987), but their derivations are reproduced here for completeness.

Consider the magnetic scalar potential ϕ which is related to the anomaly field by

$$\vec{B}_a = \vec{\nabla}\phi . \quad (A1)$$

The gradient tensor components are the second derivatives of ϕ , e.g. $g_{xy} = \partial^2\phi/\partial x\partial y$. This scalar potential can be computed if the shape and magnetization of the underlying geological source is known.

$$\phi(\vec{r}) = \int_{V_1} \frac{\vec{\nabla}_1 \cdot \vec{M}(\vec{r}_1)}{|\vec{r}_{o1}|} dV_1 - \int_{S_1} \frac{\vec{n} \cdot \vec{M}(\vec{r}_1)}{|\vec{r}_{o1}|} dS_1 . \quad (A2)$$

Here, $\vec{M}(\vec{r}_1)$ is the magnetization, \vec{r}_{o1} is the vector from the point \vec{r}_1 within the source to the point of observation \vec{r} , and \vec{n} is the outward normal vector from the surface S_1 bounding the volume V_1 .

It is clear that ϕ satisfies Laplace's equation. Also, for all real magnetic sources, ϕ approaches zero as the point of observation goes to infinity. Under these conditions, the following relations can be shown to exist between the first derivatives of a potential ϕ on a horizontal plane (Nabighian, 1984)

$$\frac{\partial\phi}{\partial x} = \frac{-1}{2\pi} \iint_{-\infty-\infty}^{\infty\infty} \frac{(x-\alpha)\partial\phi/\partial z}{[(x-\alpha)^2+(y-\beta)^2]^{3/2}} d\alpha d\beta , \quad (A3)$$

$$\frac{\partial\phi}{\partial y} = \frac{-1}{2\pi} \iint_{-\infty-\infty}^{\infty\infty} \frac{(y-\beta)\partial\phi/\partial z}{[(x-\alpha)^2+(y-\beta)^2]^{3/2}} d\alpha d\beta , \quad (A4)$$

and

$$\frac{\partial \phi}{\partial z} = \frac{1}{2\pi} \iint_{-\infty-\infty}^{\infty\infty} \frac{(x-\alpha)\partial\phi/\partial\alpha + (y-\beta)\partial\phi/\partial\beta}{[(x-\alpha)^2+(y-\beta)^2]^{3/2}} d\alpha d\beta, \quad (A5)$$

where the integration is taken over all points on the plane except the point $(x=\alpha, y=\beta)$.

Taking the partial derivative of equation (A3) with respect to x , substituting $r^2=[(x-\alpha)^2 + (y-\beta)^2]$, and noting that $\partial\phi/\partial z$ is only a function of (α, β) not (x, y) , yields the following relation

$$\begin{aligned} \frac{\partial^2 \phi}{\partial x^2} = g_{xx} &= \frac{-1}{2\pi} \iint_{-\infty-\infty}^{\infty\infty} \frac{\partial}{\partial x} \left[\frac{x-\alpha}{r^3} \right] \frac{\partial \phi}{\partial z} d\alpha d\beta \\ &= \frac{1}{2\pi} \iint_{-\infty-\infty}^{\infty\infty} \frac{\partial}{\partial \alpha} \left[\frac{x-\alpha}{r^3} \right] \frac{\partial \phi}{\partial z} d\alpha d\beta \\ &= \frac{1}{2\pi} \iint_{-\infty-\infty}^{\infty\infty} \left[\frac{\partial}{\partial \alpha} \left[\frac{x-\alpha}{r^3} \frac{\partial \phi}{\partial z} \right] - \frac{x-\alpha}{r^3} \frac{\partial^2 \phi}{\partial \alpha \partial z} \right] d\alpha d\beta. \end{aligned}$$

In the first term, the partial differentiation and integration cancel, leaving only the integrand to be evaluated at $\alpha=\pm\infty$. Thus the first term is zero. This leaves

$$g_{xx} = \frac{-1}{2\pi} \iint_{-\infty-\infty}^{\infty\infty} \frac{(x-\alpha)}{r^3} g_{\alpha z} d\alpha d\beta. \quad (A6)$$

Taking the partial derivative of equation (A3) with respect to y yields

$$\begin{aligned} \frac{\partial^2 \phi}{\partial x \partial y} = g_{xy} &= \frac{-1}{2\pi} \int_{-\infty}^{\infty} \int_{-\infty}^{\infty} \frac{\partial}{\partial y} \left[\frac{x-\alpha}{r^3} \right] \frac{\partial \phi}{\partial z} d\alpha d\beta \\ &= \frac{1}{2\pi} \int_{-\infty}^{\infty} \int_{-\infty}^{\infty} \frac{\partial}{\partial \beta} \left[\frac{x-\alpha}{r^3} \right] \frac{\partial \phi}{\partial z} d\alpha d\beta \\ &= \frac{1}{2\pi} \int_{-\infty}^{\infty} \int_{-\infty}^{\infty} \left[\frac{\partial}{\partial \beta} \left[\frac{x-\alpha}{r^3} \right] \frac{\partial \phi}{\partial z} - \frac{x-\alpha}{r^3} \frac{\partial^2 \phi}{\partial \beta \partial z} \right] d\alpha d\beta . \end{aligned}$$

The first term equals zero because the partial differentiation and integration cancel, leaving the integrand to be evaluated at $\beta = \pm \infty$. Thus

$$g_{xy} = \frac{-1}{2\pi} \int_{-\infty}^{\infty} \int_{-\infty}^{\infty} \frac{(x-\alpha)}{r^3} g_{\beta z} d\alpha d\beta . \quad (A7)$$

Taking the partial derivative of equation (A3) with respect to z yields

$$\begin{aligned} \frac{\partial^2 \phi}{\partial x \partial z} = g_{xz} &= \frac{-1}{2\pi} \int_{-\infty}^{\infty} \int_{-\infty}^{\infty} \frac{x-\alpha}{r^3} \frac{\partial^2 \phi}{\partial z^2} d\alpha d\beta \\ &= \frac{-1}{2\pi} \int_{-\infty}^{\infty} \int_{-\infty}^{\infty} \frac{(x-\alpha)}{r^3} g_{zz} d\alpha d\beta . \end{aligned} \quad (A8)$$

Using equations (A4) and (A5) instead of (A3) yield the following six auxilliary relations

$$g_{yx} = \frac{-1}{2\pi} \iint_{-\infty-\infty}^{\infty\infty} \frac{(y-\beta)}{r^3} g_{\alpha z} d\alpha d\beta , \quad (A9)$$

$$g_{yy} = \frac{-1}{2\pi} \iint_{-\infty-\infty}^{\infty\infty} \frac{(y-\beta)}{r^3} g_{\beta z} d\alpha d\beta , \quad (A10)$$

$$g_{yz} = \frac{-1}{2\pi} \iint_{-\infty-\infty}^{\infty\infty} \frac{(y-\beta)}{r^3} g_{zz} d\alpha d\beta , \quad (A11)$$

$$g_{zx} = \frac{1}{2\pi} \iint_{-\infty-\infty}^{\infty\infty} \frac{(x-\alpha)g_{\alpha\alpha} + (y-\beta)g_{\alpha\beta}}{r^3} d\alpha d\beta , \quad (A12)$$

$$g_{zy} = \frac{1}{2\pi} \iint_{-\infty-\infty}^{\infty\infty} \frac{(x-\alpha)g_{\alpha\beta} + (y-\beta)g_{\beta\beta}}{r^3} d\alpha d\beta , \quad (A13)$$

$$g_{zz} = \frac{1}{2\pi} \iint_{-\infty-\infty}^{\infty\infty} \frac{(x-\alpha)g_{\alpha z} + (y-\beta)g_{\beta z}}{r^3} d\alpha d\beta . \quad (A14)$$

Consideration of equations (A6)-(A14) reveals that all gradient components can be calculated from the measurement of g_{zz} over a horizontal plane. This is the only component for which this applies. (Both g_{xx} and g_{yy} or g_{xz} and g_{yz} are required to calculate the remaining components.)

APPENDIX B

RELATIONS BETWEEN THE TOTAL-FIELD, THE TOTAL-FIELD
DERIVATIVES, AND THE GRADIENT TENSOR: FREQUENCY DOMAIN

The magnetic field due to a geological source is a vector quantity, denoted here by \vec{B}_a . The total-field anomaly (tf) due to this source is a scalar quantity equal to the projection of the vector field in the direction of the Earth's field (\hat{B}_{earth}).

$$tf = \vec{B}_a \cdot \hat{B}_{\text{earth}} . \quad (B1)$$

The total-field derivatives are

$$G_x = \frac{\partial}{\partial x} (\vec{B}_a \cdot \hat{B}_{\text{earth}}) = \frac{\partial B_x}{\partial x} \hat{B}_{\text{ex}} + \frac{\partial B_y}{\partial x} \hat{B}_{\text{ey}} + \frac{\partial B_z}{\partial x} \hat{B}_{\text{ez}} , \quad (B2)$$

$$G_y = \frac{\partial}{\partial y} (\vec{B}_a \cdot \hat{B}_{\text{earth}}) = \frac{\partial B_x}{\partial y} \hat{B}_{\text{ex}} + \frac{\partial B_y}{\partial y} \hat{B}_{\text{ey}} + \frac{\partial B_z}{\partial y} \hat{B}_{\text{ez}} , \quad (B3)$$

$$G_z = \frac{\partial}{\partial z} (\vec{B}_a \cdot \hat{B}_{\text{earth}}) = \frac{\partial B_x}{\partial z} \hat{B}_{\text{ex}} + \frac{\partial B_y}{\partial z} \hat{B}_{\text{ey}} + \frac{\partial B_z}{\partial z} \hat{B}_{\text{ez}} , \quad (B4)$$

where it is assumed that the the Earth's field is constant over the region of interest. \hat{B}_{ex} , \hat{B}_{ey} , and \hat{B}_{ez} are the x,y, and z direction cosines of the Earth's field vector. Using the symmetry properties of the gradient tensor, these equations can be rewritten in the form

$$G_x = \hat{B}_{\text{ex}} g_{xx} + \hat{B}_{\text{ey}} g_{xy} + \hat{B}_{\text{ez}} g_{xz} , \quad (B5)$$

$$G_y = \hat{B}_{\text{ex}} g_{xy} + \hat{B}_{\text{ey}} g_{yy} + \hat{B}_{\text{ez}} g_{yz} , \quad (B6)$$

$$G_z = \hat{B}_{\text{ex}} g_{xz} + \hat{B}_{\text{ey}} g_{yz} - \hat{B}_{\text{ez}} (g_{xx} + g_{yy}) . \quad (B7)$$

The relations between the total-field, its derivatives, and the gradient tensor components can also be formulated in the frequency domain.

The two-dimensional Fourier transform and its inverse are defined as

$$F(k_x, k_y) = \iint_{-\infty-\infty}^{\infty\infty} f(x, y) e^{-i(k_x x + k_y y)} dx dy , \quad (B8)$$

and

$$f(x, y) = \frac{1}{4\pi^2} \iint_{-\infty-\infty}^{\infty\infty} F(k_x, k_y) e^{i(k_x x + k_y y)} dk_x dk_y . \quad (B9)$$

Throughout the remainder of this work, the Fourier transform of a function $f(x, y)$ will be denoted $\text{FFT}(f)$.

The relationships between the Fourier transforms of the total-field and the horizontal and vertical gradients are (Nabighian 1984)

$$\text{FFT}(G_z) = |k| \times \text{FFT}(tf) , \quad (B10)$$

$$\text{FFT}(G_z) = -i \frac{k_x}{k} \text{FFT}(G_x) - i \frac{k_y}{k} \text{FFT}(G_y) , \quad (B11)$$

where $k^2 = k_x^2 + k_y^2$. Thus, the vertical derivative (G_z) can be calculated from either a grid of total-field values (tf) and equation (B10), or a grid of horizontal derivative values (G_x and G_y) and equation (B11).

The relationships between the Fourier transforms of the various gradient tensor components can be calculated from the integral relations given in Appendix A. Calculation of the Fourier transform of g_{xx} from that

of g_{xz} illustrates the method. Starting from equation (A6)

$$g_{xx} = \frac{-1}{2\pi} \iint_{-\infty-\infty}^{\infty\infty} \frac{(x-\alpha)}{r^3} g_{\alpha z} d\alpha d\beta .$$

Thus,

$$\begin{aligned} \text{FFT}(g_{xx}) &= \frac{-1}{2\pi} \iint_{-\infty-\infty}^{\infty\infty} dx dy e^{-i(k_x x + k_y y)} \iint_{-\infty-\infty}^{\infty\infty} \frac{(x-\alpha)}{r^3} g_{\alpha z} d\alpha d\beta \\ &= \frac{-1}{2\pi} \iint_{-\infty-\infty}^{\infty\infty} d\alpha d\beta g_{\alpha z} \iint_{-\infty-\infty}^{\infty\infty} \frac{(x-\alpha)}{r^3} e^{-i(k_x x + k_y y)} dx dy \\ &= \frac{-1}{2\pi} \iint_{-\infty-\infty}^{\infty\infty} d\alpha d\beta \left\{ g_{\alpha z} e^{-i(k_x \alpha + k_y \beta)} \times \right. \\ &\quad \left. \iint_{-\infty-\infty}^{\infty\infty} \frac{(x-\alpha)}{r^3} e^{-i(k_x (x-\alpha) + k_y (y-\beta))} d(x-\alpha) d(y-\beta) \right\} . \quad (\text{B12}) \end{aligned}$$

The second set of integrals can be broken down into integrals involving sines and cosines multiplied by a rational function of $(x-\alpha)$ and $(y-\beta)$. These integrals can be found in published tables; the result is $-2\pi i k_x / k$.

The first integral is just the Fourier transform of g_{xz} . Thus

$$\text{FFT}(g_{xx}) = \frac{ik_x}{k} \text{FFT}(g_{xz}) \quad . \quad (\text{B13})$$

Similar manipulations will yield the frequency domain equations (B14)-(B21) from the space domain equations (A7)-(A14).

$$\text{FFT}(g_{xy}) = \frac{ik_x}{k} \text{FFT}(g_{yz}) \quad , \quad (\text{B14})$$

$$\text{FFT}(g_{xz}) = \frac{ik_x}{k} \text{FFT}(g_{zz}) \quad , \quad (\text{B15})$$

$$\text{FFT}(g_{yx}) = \frac{iky}{k} \text{FFT}(g_{xz}) \quad , \quad (\text{B16})$$

$$\text{FFT}(g_{yy}) = \frac{iky}{k} \text{FFT}(g_{yz}) \quad . \quad (\text{B17})$$

$$\text{FFT}(g_{yz}) = \frac{iky}{k} \text{FFT}(g_{zz}) \quad , \quad (\text{B18})$$

$$\text{FFT}(g_{zx}) = -\frac{ik_x}{k} \text{FFT}(g_{xx}) - \frac{iky}{k} \text{FFT}(g_{xy}) \quad , \quad (\text{B19})$$

$$\text{FFT}(g_{zy}) = -\frac{ik_x}{k} \text{FFT}(g_{xy}) - \frac{iky}{k} \text{FFT}(g_{yy}) \quad , \quad (\text{B20})$$

$$\text{FFT}(g_{zz}) = -\frac{ik_x}{k} \text{FFT}(g_{xz}) - \frac{iky}{k} \text{FFT}(g_{yz}) \quad , \quad (\text{B21})$$

Taking the two-dimensional Fourier transform of equations (B5)-(B7), and using equations (B13)-(B21) to redefine the Fourier transforms of the tensor gradient components in terms of $\text{FFT}(g_{zz})$, yields the relationships between the Fourier transforms of the horizontal and vertical derivatives of the total-field and g_{zz} .

$$\text{FFT}(G_x) = \left[-\frac{k_x k_x}{k^2} \hat{B}_{ex} - \frac{k_x k_y}{k^2} \hat{B}_{ey} + i \frac{k_x}{k} \hat{B}_{ez} \right] \text{FFT}(g_{zz}) , \quad (\text{B22})$$

$$\text{FFT}(G_y) = \left[-\frac{k_x k_y}{k^2} \hat{B}_{ex} - \frac{k_y k_y}{k^2} \hat{B}_{ey} + i \frac{k_y}{k} \hat{B}_{ez} \right] \text{FFT}(g_{zz}) , \quad (\text{B23})$$

$$\text{FFT}(G_z) = \left[i \frac{k_x}{k} \hat{B}_{ex} + i \frac{k_y}{k} \hat{B}_{ey} + \hat{B}_{ez} \right] \text{FFT}(g_{zz}) . \quad (\text{B24})$$

The last equation can be rearranged to yield the following relation

$$\text{FFT}(g_{zz}) = \left[\frac{-k^2 \hat{B}_{ez} - ik(k_x \hat{B}_{ex} + k_y \hat{B}_{ey})}{(k_x \hat{B}_{ex} + k_y \hat{B}_{ey})^2 + k^2 \hat{B}_{ez}^2} \right] \text{FFT}(G_z) . \quad (\text{B25})$$

Finally, equations (B11) and (B25) can be used to relate the Fourier transform of the gradient tensor component g_{zz} to that of the horizontal derivatives of the total-field.

$$\begin{aligned} \text{FFT}(g_{zz}) = & \left[\frac{-k_x(k_x \hat{B}_{ex} + k_y \hat{B}_{ey}) - ik_x k \hat{B}_{ez}}{(k_x \hat{B}_{ex} + k_y \hat{B}_{ey})^2 + k^2 \hat{B}_{ez}^2} \right] \text{FFT}(G_x) \\ & + \left[\frac{-k_y(k_x \hat{B}_{ex} + k_y \hat{B}_{ey}) - i k_y k \hat{B}_{ez}}{(k_x \hat{B}_{ex} + k_y \hat{B}_{ey})^2 + k^2 \hat{B}_{ez}^2} \right] \text{FFT}(G_y) . \quad (\text{B26}) \end{aligned}$$

Equations (B25) and (B26) are stable for all values of k_x and k_y except $k_x=k_y=0$. Since this dc value should be zero for all finite, bounded sources, equations (B25) and (B26) can be used to generate the Fourier transform of the tensor component g_{zz} from either a grid of vertical (G_z) or horizontal (G_x and G_y) total-field derivative data respectively. Equations (B14)-(B21) can then be used to generate the remaining tensor components.

It should be noted that the grid spacing determines the maximum values of k_x and k_y and the total number of data points divided by the grid spacing determines the resolution of k_x and k_y in the two-dimensional digital Fourier transform. Although equidistant grid spacing along both axes may be preferable for ease of analysis, it is not required in order to apply equations (B25) or (B26).

An iterative deconvolution technique for calculating the magnetization in a layer of material with known topography, based on a set of magnetic measurements above that layer, has been developed by Parker and Huestis (1974). The method is described here for completeness.

First, assume that the magnetic source is a horizontal layer of magnetized material extending to infinity in both dimensions, and that the magnetization vector points in the same direction everywhere. In addition, assume that the magnetization amplitude is allowed to vary with horizontal position but not with depth. i.e.

$$\vec{M} = M(x,y)\hat{M} . \quad (C1)$$

Although the direction \hat{M} is unknown, the magnetization near sea-floor spreading centres is thought to be predominantly either parallel or anti-parallel to the direction of the Earth's field at present. Thus a positive $M(x,y)$ refers to magnetization parallel to the Earth's field, and a negative $M(x,y)$ refers to magnetization anti-parallel to the Earth's field. For simplicity, choose $z=0$ to be the upper surface of the horizontal source layer.

The total-field (tf) measured at any point (x,y) on a plane z_0 above the source layer is the summation of the signals due to each infinitesimal vertical prism of volume (thickness $\times dx' \times dy'$). The signal (S) from each vertical prism depends only on the relative location of the prism and the observation point and its magnetization $M(x',y')$.

$$tf(x,y) = \iint_{-\infty-\infty}^{\infty\infty} M(x',y') S(x-x',y-y',z_0) dx'dy' . \quad (C2)$$

Taking the Fourier transform of equation (C2) yields

$$\text{FFT}(tf) = \iint_{-\infty-\infty}^{\infty\infty} e^{-i(k_x x + k_y y)} \left\{ \iint_{-\infty-\infty}^{\infty\infty} M(x', y') S(x-x', y-y', z_0) dx' dy' \right\} dx dy . \quad (\text{C3})$$

The exponential term can be expanded as

$$e^{-i(k_x x + k_y y)} = e^{-i(k_x (x-x') + k_y (y-y'))} e^{-i(k_x x' + k_y y')} , \quad (\text{C4})$$

and the derivatives rewritten as

$$dx = d(x-x') , \quad (\text{C5a})$$

$$dy = d(y-y') . \quad (\text{C5b})$$

Therefore

$$\begin{aligned} \text{FFT}(tf) &= \iint_{-\infty-\infty}^{\infty\infty} e^{-i(k_x (x-x') + k_y (y-y'))} e^{-i(k_x x' + k_y y')} \times \\ &\quad \left\{ \iint_{-\infty-\infty}^{\infty\infty} M(x', y') S(x-x', y-y', z_0) dx' dy' \right\} d(x-x') d(y-y') \\ &= \iint_{-\infty-\infty}^{\infty\infty} e^{-i(k_x (x-x') + k_y (y-y'))} S(x-x', y-y', z_0) d(x-x') d(y-y') \end{aligned}$$

$$\begin{aligned} & \times \iint_{-\infty-\infty}^{\infty\infty} e^{-i(k_x x' + k_y y')} M(x', y',) dx' dy' \\ & = \text{FFT}(S) \times \text{FFT}(M) . \end{aligned} \tag{C6}$$

Equation (C6) indicates that the Fourier transform of the measured magnetic field is the product of the Fourier transform of the field due to a single prism and the Fourier transform of the magnetization. The magnetization can be recovered by solving equation (C6)

$$M(x, y) = \text{FFT}^{-1}(\text{FFT}(tf)/\text{FFT}(S)) . \tag{C7}$$

If the magnetic source layer is no longer constrained to lie in a horizontal plane but now contains some topographic relief ($\Delta z(x', y')$), then equation (C2) can be expanded in a Taylor series.

$$\begin{aligned} tf(x, y) &= \iint_{-\infty-\infty}^{\infty\infty} M(x', y') S(x-x', y-y', z_0) dx' dy' \\ &+ \iint_{-\infty-\infty}^{\infty\infty} \frac{\partial}{\partial z} [M(x', y') S(x-x', y-y', z_0)] \Big|_{z=z_0} \Delta z(x', y') dx' dy' \\ &+ \iint_{-\infty-\infty}^{\infty\infty} \frac{1}{2} \frac{\partial^2}{\partial z^2} [M(x', y') S(x-x', y-y', z_0)] \Big|_{z=z_0} \Delta z^2(x', y') dx' dy' \\ &+ \dots \end{aligned}$$

$$= \iint_{-\infty-\infty}^{\infty\infty} M(x', y') \left[1 + \sum_{n=1}^{\infty} \frac{1}{n!} \frac{\partial}{\partial z^n} \right] \Bigg|_{z=z_0} S(x-x', y-y', z_0) \Delta z^n(x', y') dx' dy' . \quad (C8)$$

Taking the Fourier transform of both sides yields

$$\text{FFT}(tf) = \text{FFT}(M) \times \text{FFT}(S) \Bigg|_{z=z_0} + \sum_{n=1}^{\infty} \text{FFT}(M \Delta z^n) \frac{1}{n!} \left[\frac{\partial}{\partial z^n} \text{FFT}(S) \right] \Bigg|_{z=z_0} . \quad (C9)$$

However,

$$\begin{aligned} \frac{\partial}{\partial z^n} \text{FFT}(S) &= (k_x^2 + k_y^2)^{n/2} \text{FFT}(S) \\ &= |k^n| \text{FFT}(S) . \end{aligned} \quad (C10)$$

Therefore,

$$\text{FFT}(tf) = \text{FFT}(M) \times \text{FFT}(S) \Bigg|_{z=z_0} + \sum_{n=1}^{\infty} \text{FFT}(M \Delta z^n) \frac{|k^n|}{n!} \text{FFT}(S) \Bigg|_{z=z_0} . \quad (C11)$$

This equation can be rearranged into an iterative expression for the magnetization

$$M_i(x, y) = \text{FFT}^{-1} \left\{ \text{FFT}(M_0) - \sum_{n=1}^{\infty} \frac{|k^n|}{n!} \text{FFT}(M_{i-1} \Delta z^n) \right\} , \quad (C12)$$

where

$$\text{FFT}(M_0) = \frac{\text{FFT}(tf)}{\text{FFT}(S)} \Bigg|_{z=z_0} . \quad (C13)$$

In practice, the summation is cut off at some value N usually found by trial and error. Equation (C12) has been derived previously by Parker and Huestis (1974).

The non-uniqueness problem in magnetic field inversion can be seen in equation (C11). Consider a distribution of magnetization $A(x,y)$ which produces no measurable signal on the plane of observation. Equation (C11) becomes

$$0 = \text{FFT}(A) \times \text{FFT}(S) \Big|_{z=z_0} + \sum_{n=1}^{\infty} \text{FFT}(A\Delta z^n) \frac{|k^n|}{n!} \text{FFT}(S) \Big|_{z=z_0} . \quad (\text{C14})$$

Notice that in the case $\Delta z=0$, equation (C14) reduces to the well known result that a horizontal layer with constant magnetization produces no magnetic field. When $\Delta z \neq 0$, equation (C14) can be rearranged to form an iterative solution for $A_i(x,y)$.

$$A_i(x,y) = - \text{FFT}^{-1} \left\{ \sum_{n=1}^{\infty} \frac{|k^n|}{n!} \text{FFT}(A_{i-1}\Delta z^n) \right\} . \quad (\text{C15})$$

where A_0 is a constant. For simplicity, choose $A_0=1$. Again the summation is cut off at some value N in any practical algorithm. $A_i(x,y)$ is termed the "annihilator" by Parker and Huestis.

Because the distribution $A(x,y)$ causes no measurable signal, $A(x,y)$ multiplied by any constant and added to $M(x,y)$ will produce the same field measurements as $M(x,y)$ alone. Thus there is a whole family of solutions to the inverse problem

$$M_i'(x,y) = M_i(x,y) + cA_i(x,y) . \quad (\text{C16})$$

REPORT NO.: Technical Memorandum 88-21

TITLE: Crustal Magnetization and Gradient Tensor
Component Maps of the Northern Juan de Fuca Ridge

DATED: November 1988

AUTHOR: J. Bradley Nelson

SECURITY GRADING: UNCLASSIFIED

3-DSIS

Circulate to:

DRDM

DRDA

1-CRAD

1-DGRD Ops

1-DRDA 2

Attn: LCol. J. Bauer

1-NAE

Attn: Mr. Doug Hardwick

DOCUMENT CONTROL DATA

(Security classification of title, body of abstract and indexing annotation must be entered when the overall document is classified)

1 ORIGINATOR (the name and address of the organization preparing the document. Organizations for whom the document was prepared, e.g. Establishment sponsoring a contractor's report, or tasking agency, are entered in section 8) Defence Research Establishment Pacific		2 SECURITY CLASSIFICATION (overall security classification of the document including special warning terms if applicable) Unclassified	
3 TITLE (the complete document title as indicated on the title page. Its classification should be indicated by the appropriate abbreviation (S,C,R or U) in parentheses after the title) Crustal Magnetization and Gradient Tensor Component Maps of the Northern Juan de Fuca Ridge. (U)			
4 AUTHORS (Last name, first name, middle initial) J. Bradley Nelson			
5 DATE OF PUBLICATION (month and year of publication of document) November 1988	6a. NO OF PAGES (total containing information include Annexes, Appendices, etc) 49	6b NO OF REFS (total cited in document) 12	
7 DESCRIPTIVE NOTES (the category of the document, e.g. technical report, technical note or memorandum. If appropriate, enter the type of report, e.g. interim, progress, summary, annual or final. Give the inclusive dates when a specific reporting period is covered.) Technical Memorandum			
8 SPONSORING ACTIVITY (the name of the department project office or laboratory sponsoring the research and development. Include the address)			
9a PROJECT OR GRANT NO (if appropriate, the applicable research and development project or grant number under which the document was written. Please specify whether project or grant) Project 37A02		9b CONTRACT NO (if appropriate, the applicable number under which the document was written)	
10a ORIGINATOR'S DOCUMENT NUMBER (the official document number by which the document is identified by the originating activity. This number must be unique to this document) Technical Memorandum 88-21		10b OTHER DOCUMENT NOS (Any other numbers which may be assigned this document either by the originator or by the sponsor)	
11 DOCUMENT AVAILABILITY (any limitations on further dissemination of the document, other than those imposed by security classification) <input checked="" type="checkbox"/> Unlimited distribution <input type="checkbox"/> Distribution limited to defence departments and defence contractors, further distribution only as approved <input type="checkbox"/> Distribution limited to defence departments and Canadian defence contractors, further distribution only as approved <input type="checkbox"/> Distribution limited to government departments and agencies, further distribution only as approved <input type="checkbox"/> Distribution limited to defence departments, further distribution only as approved <input type="checkbox"/> Other (please specify)			
12 DOCUMENT ANNOUNCEMENT (any limitation to the bibliographic announcement of this document. This will normally correspond to the Document Availability (11). However, where further distribution (beyond the audience specified in 11) is possible, a wider announcement audience may be selected) NONE			

13 ABSTRACT (a brief and factual summary of the document. It may also appear elsewhere in the body of the document itself. It is highly desirable that the abstract of classified documents be unclassified. Each paragraph of the abstract shall begin with an indication of the security classification of the information in the paragraph (unless the document itself is unclassified) represented as (S), (C), (R), or (U). It is not necessary to include here abstracts in both official languages unless the text is bilingual.)

SEE REPORT

61396
89-03499

14 KEYWORDS, DESCRIPTORS or IDENTIFIERS (technically meaningful terms or short phrases that characterize a document and could be helpful in cataloguing the document. They should be selected so that no security classification is required. Identifiers, such as equipment model designation, trade name, military project code name, geographic location may also be included. If possible keywords should be selected from a published thesaurus, e.g. Thesaurus of Engineering and Scientific Terms (TEST) and that thesaurus-identified. If it is not possible to select indexing terms which are Unclassified, the classification of each should be indicated as with the title.)

Juan de Fuca Ridge

Magnetization

Magnetic Gradient

Magnetic Anomaly